Utah State University

DigitalCommons@USU

5-2017

Characterization of the Thermal Resistance of Grain Boundaries of Cerium Oxide

Jesse Spackman
Utah State University

UtahStateUniversity
MERRILL-CAZIER LIBRARY

CHARACTERIZATION OF THE THERMAL RESISTANCE OF GRAIN

BOUNDARIES OF CERIUM OXIDE

by

Jesse Spackman

A thesis submitted in partial fulfillment
of the requirements for the degree

of

MASTER OF SCIENCE

in

Mechanical Engineering

Approved:

_____   _____
Heng Ban, Ph.D.   Nicholas Roberts, Ph.D.
Major Professor   Committee Member

_____   _____
Thomas Fronk, Ph.D.   Mark R. McLellan, Ph.D.
Committee Member   Vice President for Research and
                                         Dean of the School of Graduate Studies

UTAH STATE UNIVERSITY
Logan, Utah

2017

ABSTRACT

Characterization of the Thermal Resistance of Grain

Boundaries of Cerium Oxide

by

Jesse Spackman, Master of Science

Utah State University, 2017

Major Professor: Dr. Heng Ban
Department: Mechanical and Aerospace Engineering

An important aspect in the thermal transport process in many polycrystalline

materials is the presence of a high density of grain boundaries and crystal interfaces.

These interfaces present additional phonon scattering features that have few well-defined

characteristics. Because these interfaces serve as phonon scattering sites, they inhibit

heat flow and act as thermal resistors. This resistance from grain boundaries and other

interfaces in general is referred to as the Kapitza resistance. Nuclear fuels are

polycrystalline materials and are subjected to extreme heat and irradiated conditions that

can lead them to experience sharp local changes in temperature and thermal properties.

A better understanding of these grain boundaries and the role they play in transferring

heat can help better predict nuclear fuel performance and improve nuclear reactor

efficiency and safety. The study of the thermal resistance across crystal interfaces and

their potential influence on nuclear fuels is a topic that has received relatively little

attention. Although the thermal resistance arising from a single grain boundary is generally small, the total resistance generated from many grain boundaries has a large influence on the material on a macro scale. The smaller the average size of the grain, the more prevalent the number of grain boundaries will become, which in turn reduces the total thermal conductivity of the material. For this study, the heat flow across naturally occurring crystalline interfaces was observed in order to characterize the Kapitza resistance across grain boundaries. The method used is the spatial-scan photothermal reflectance technique (SSPRT). The sample material was Cerium Oxide (CeO_2), used because of its similar properties to Uranium Oxide (UO_2), which is a popular material in nuclear fuel.

The average interfacial thermal resistance measured in this thesis study was $9.88 \cdot 10^{-9} \; m^2 K/W$. Although there exists a level of experimental uncertainty, this measured value is relatively consistent with results from other studies. There was also a wide variety of grain boundary resistances measured in the range of $1.7 \cdot 10^{-9} \; m^2 K/W$ to $5 \cdot 10^{-8} \; m^2 K/W$. This large range is attributed to the different types of grain boundaries present. Low-angle boundaries are expected to limit heat flow less than high-angle grain boundaries or boundaries with more voids.

(103 pages)

PUBLIC ABSTRACT

Characterization of the Thermal Resistance of Grain

Boundaries of Cerium Oxide

Jesse Spackman, Master of Science

Many materials are made up of small crystals, or grains. Grain boundaries are the interfaces between two grains and affect the flow of heat through the material. These interfaces serve to interfere with the energy carriers by scattering or disrupting them. Because of the negative effect these interfaces have on these energy carriers, they inhibit heat flow and act as thermal resistors. The thermal boundary resistance between two grains of the same material is sometimes referred to as the Kapitza resistance, although this term is also used to describe the thermal resistance between solid/solid interfaces of different materials or solid/liquid interfaces. A better understanding of the heat transport process on a micro-scale is especially relevant to nuclear energy applications. Nuclear fuels are polycrystalline materials that experience large heat differences over small distances. An improved understanding of these grain boundaries and the role they play in transferring heat can help better predict nuclear fuel performance and improve nuclear reactor efficiency and safety.

The study of the thermal resistance across crystal interfaces and their potential influence on nuclear fuels is a topic that has received relatively little attention. While the thermal resistance across a single grain boundary is rather small, the total resistance generated from many grain boundaries can have a big impact on the material. Smaller

grains mean there are more interfaces, which will result in a lower overall thermal conductivity.

For this study, Kapitza resistance across individual grain boundaries was measured using a laser-based measurement technique. The sample material was Cerium Oxide. It was used because of its similar properties to Uranium Oxide, which is a popular material used in nuclear fuel. The average interfacial thermal resistance measured at room temperature in this thesis study was $9.88 \cdot 10^{-9} \, m^2 K/W$. The average measured value fit in an accepted range from other results found in similar studies.

ACKNOWLEDGMENTS

I would first and foremost like to thank my advising professor, Dr. Ban, for all of his help and support over these past few years. It is because of his motivation and influence that I was even able to get to this stage in my academic career. Were it not for his unwavering support, I wouldn't have accomplished my goals. Although his office number is 419E, he will forever be #1 in the hearts of his students. Words cannot adequately express the deepest gratitude and respect that I have for this magnanimous and altruistic man. In the future years to come, I will look back fondly to the time that I spent at USU under his great tutelage. I could not have asked for a better instructor and mentor. There are many titles that he carries, but the one that I will cherish the most is the title of friend.

I would also like to thank my lab mates and the staff at Utah State University for their selfless help. A special thanks goes to Zilong Hua. I owe him a lot for his guidance and his teaching. I also want to thank Levi Gardner, Tyson Watkins, Zhuorui Song, Yuefang Dong, Zeke Villareal, Tate Shorthill, Kurt Harris, and Nathaniel Scheelke. We spent many good times together in and out of the lab and they made my experience at Utah State all the more enjoyable. They are not only my coworkers, but also my friends. I also owe a thanks to many other friends outside of school including Travis Colvin, Colton Hirschi, Montana Thompson, Marcus Ritter, Landon Hillyard, and Devan Radle. Their examples and motivation helped me more than they know.

A major thanks also needs to be expressed to the Department of Energy and the Nuclear Energy University Program. It is due to their support that I was able to fund my graduate studies.

Finally, I would like to express my gratitude to my biggest support group, my family. My parents, Bruce and Terri Spackman, have been instrumental in my academic achievements and are truly my biggest fans. I owe all of my success to them and their unwavering support in all of my endeavors. I would also like to thank my siblings for their help and encouragement that they have extended throughout the years.

Jesse Spackman

CONTENTS

LIST OF TABLES

LIST OF FIGURES

ACRONYMS

AMM   Acoustic Mismatch Model

AOM   Acousto-optic modulator

CCD   Charged-couple device

DDM   Diffusive Mismatch Model

EBSD Electron backscatter diffraction

IPF   Inverse Pole Figure

MD   Molecular dynamics

SSPRT Spatial-scan photothermal reflectance technique

CeO_2 Cerium Oxide

UO_2 Uranium Oxide

PuO_2 Plutonium Oxide

NOMENCLATURE

A	Area $[m^2]$
c	Specific heat $[J/kg \cdot K]$
c_f	Specific heat of the film $[J/kg \cdot K]$
c_p	Constant pressure specific heat $[J/kg \cdot K]$
c_v	Constant volume specific heat $[J/kg \cdot K]$
d	Average grain size $[m]$
D	Thermal diffusivity $[m^2/s]$
D_{eff}	Effective thermal diffusivity $[m^2/s]$
D_f	Thermal diffusivity of the film $[m^2/s]$
D_s	Thermal diffusivity of the substrate $[m^2/s]$
f	Frequency [Hz]
$\dot{g}$	Energy generation rate $[W/m^3]$
G_k	Kapitza thermal conductivity $[W/m^2 \cdot K]$
k	Thermal conductivity $[W/m \cdot K]$
k_B	Boltzmann constant $[J/K]$
k_f	Thermal conductivity of the film $[W/m \cdot K]$
k_i	Intrinsic thermal conductivity $[W/m \cdot K]$
k_s	Thermal conductivity of the substrate $[W/m \cdot K]$
l	Phonon mean free path $[m]$
l_k	Kapitza length $[m]$
L	Length $[m]$
L_{th}	Thermal diffusion length $[m]$
p	Hankel transformation variable
P_0	Heat source intensity $[W]$
q''	Heat flux $[W/m^2]$

R Optical reflectivity

R_f Optical reflectivity of the film

R_k Kapitza resistance $[m^2 \cdot K/W]$

R_s Optical reflectivity of the substrate

R_{th} Thermal resistance $[K/W]$

T Temperature [K]

T_f Temperature of the film [K]

T_{gb} Temperature difference across grain boundary [K]

T_s Temperature of the substrate [K]

t time [s]

v Velocity $[m/s]$

v_s Sound velocity $[m/s]$

α Frequency dependent transmission coefficient

η_1 Thermal phase profile characteristic [deg]

η_2 Phase drop [deg]

ρ Density $[kg/m^3]$

ρ_f Density of the film $[kg/m^3]$

φ Phase lag [deg]

ω Angular frequency [Hz]

ω_D Debye frequency [Hz]

CHAPTER 1

INTRODUCTION

The thermal resistance quantification at interfaces between crystallites, the role

that they play on the heat flow through a solid, and the effect that they have on the overall

thermal conductivity of a solid has yet to be explored in great detail in some materials.

While this topic has been studied extensively for interfaces separating two different

materials, the thermal boundary resistance between grains of the same material has not

received as much attention. The purpose of this master's thesis is to evaluate the thermal

resistance across grain boundaries of Cerium Oxide and discuss its overall influence on

the solid. In this chapter, the essentials of heat conduction are discussed with emphasis

on certain parameters including thermal conductivity, phonon transport, thermal

resistance, thermal boundary conductance, thermal diffusivity, and thermal diffusion

length, as well as an introduction to Cerium Oxide and grain boundaries.

1.1 Heat Transfer

Heat transfer is the flow of thermal energy in a system due to a spatial

temperature difference. The rate at which the heat is transferred is dependent on the

material's properties and on the temperatures of the systems through which the heat is

flowing. There are three fundamental modes of heat transfer; conduction, convection,

and thermal radiation. Conduction describes the transfer of heat across a stationary

medium such as a solid or a liquid. Convection refers to heat exchanged between a

moving fluid and a surface when they are at different temperatures. Radiation describes

heat transfer in the form of energy emitted by electromagnetic waves. Radiation is the only mode of heat transfer that does not require a medium to exchange heat.

1.1.1 Thermal Conductivity

Conduction can be considered as the transfer of energy from higher energetic particles to less energetic ones due to the microscopic collisions and interactions between the particles within a body. Higher temperatures typically result in higher molecular energies. With the presence of a temperature gradient, the flow of energy by conduction will then ensue in the direction of decreasing temperature. The rate at which energy is conducted is a function of material properties and the temperature gradient. For one dimensional (1D) conduction in the x direction, the rate at which heat is transferred can be quantified by Fourier's Law [1]:

$$q_x'' = -k\frac{dT}{dx} \tag{1.1}$$

where q_x'' is the heat flux in the x direction per unit area perpendicular to the direction of heat transfer. The proportionality ratio k is the thermal conductivity with SI units of $W/m \cdot K$ and is a property of the material.

Thermal conductivity is the most important thermal transport property when discussing conduction. It is the physical factor that quantifies a given material's ability to conduct thermal energy. This property also varies widely in materials. Metals typically have higher values of thermal conductivity while ceramics and other non-metals have relatively lower values. The large discrepancy in different conductivities in varying materials can be attributed to the differences in microstructure. Metals have many free

electrons which act as the primary carriers of thermal energy. While heat is also transferred by other methods in metals, it is small in comparison to the energy carried by free electrons. Non-metal crystals do not have the abundance of free electrons and so must rely on other mechanisms, namely phonons, to transfer heat.

1.1.2 Phonon Transport

The transportation of thermal energy in metals and non-metals alike requires carrier particles or waves to move energy from one place to another. The movement of the individual atoms in the crystal lattice can be represented in the harmonic approximation as an ensemble of excitations. When quantized, these excitations are defined as phonons. A phonon represents a quantum mechanical description of the vibrational energy that arises from uniformly oscillating atoms or molecules within a crystal. Because a packet of these waves can travel with a definite energy and momentum through the crystal, they can be treated as particles.

Phonons propagate through the material carrying energy, which in turn contributes to the thermal conductivity. In principle, a purely harmonic solid has an infinite thermal conductivity. This is because within the purely harmonic picture of lattice vibrations, phonons are the quantum eigenstates of the atomic system and therefore they can propagate without dissipation. However, solids do in fact have a finite thermal conductivity because dissipation occurs by phonon scattering off of either each other or from imperfections of the lattice such as dislocation, point defects, or of particular interest in this study, grain interfaces.

The thermal conductivity can be described by the Debye equation, which is directly related to phonon velocity, phonon mean free path, and utilizes the kinetic theory. The phonons are also represented as pseudo-particles traveling through a solid. The Debye equation is the following:

$$k = \frac{1}{3} c_v v l \qquad (1.2)$$

Where c_v is the heat capacity at constant volume, v is the velocity of the phonons, and l is the phonon mean free path – the characteristic length for scattering of phonons off each other or off a structural defect [2].

In non-metals, phonons are considered to be the primary thermal energy carriers. While phonons also act as energy carriers in metals, their contribution to the overall heat flow is so small in comparison to that of electron carriers that it can often be neglected, especially in pure metals [3].

1.1.3 Thermal Resistance

Another thermal property, and one that is of particular importance in this study, is thermal resistance. It defines the ability of a material to resist the flow of heat and is a function of thermal conductivity and the length of the material. Because of its inverse relation to conductivity, materials with high conductivity have low values of resistance while materials with low values of conductivity have high values of resistance. The SI unit for thermal resistance is K/W. The concept of thermal resistance is especially useful when analyzing a system with multiple materials and geometries. The analogy to electrical circuits is obvious as the thermal system can be analyzed much like an electric

circuit would. The expression of thermal resistance for conduction for a plane wall is

$R_{th} = L/kA$, where L is length and A is area.

1.1.4   Thermal Boundary Conductance and Resistance

The thermal property of most interest in this thesis study is the thermal boundary resistance, or Kapitza resistance. Its reciprocal is the Kapitza conductance, which for a unit area at the interface, is defined as the ratio of the heat flux to the temperature discontinuity at the interface. The SI units of the Kapitza conductance is $W/m^2 \cdot K$. Similar to the overall thermal conductivity, the Kapitza conductance is directly influenced by energy carriers, or phonons. The Kapitza conductance is characterized by the number of energy carriers incident on the interface, the energy being transported by the carriers, and the probability of each phonon that it will be transferred across the boundary [4]. A schematic representation of the temperature difference across grain boundaries can be seen in Figure 1.1.
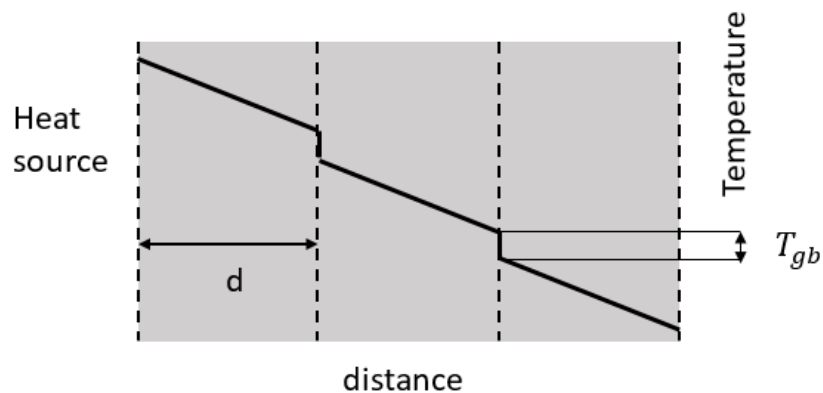
Figure 1.1: Schematic illustration of the 1D temperature profile across a multi-grain sample in response to an applied heat flux. Dashed lines represent grain interfaces. The Kapitza resistance to thermal transport results in a temperature discontinuity T_{gb} at every grain boundary or interface.

1.1.5   Thermal Diffusivity

An important material property that plays a large role in heat transfer is thermal diffusivity. It is defined as the ratio of the thermal conductivity to the heat capacity and has units of m^2/s:

$$D = \frac{k}{\rho c_p} \qquad (1.3)$$

Thermal diffusivity can be described as the measurement of thermal inertia. It measures the ability of a material to conduct heat relative to its ability to store heat. A substance with a higher thermal diffusivity will allow heat to flow more rapidly through it because it conducts heat quickly relative to its volumetric heat capacity.

1.1.6   Thermal Wave and Thermal Diffusion Length

Other important concepts to heat transfer and that have particular relevance in this study are those of the thermal wave and the thermal diffusion length. The thermal wave concept was introduced by Carslaw and Jaeger [5]. It defines the temperature profile derived from the thermal conduction equation with a harmonic heat source as a wave-like function. This means the temperature profile moves in both space and time as a thermal wave if the heating source fluctuates periodically. This concept is widely used to describe temperature oscillations produced by harmonic heat sources.

In solid materials, the range or depth of penetration of the thermal wave as it propagates from the heat source is known as the thermal diffusion length. It describes the distance at which an appreciable energy transfer takes place and is defined as $L_{th} = \sqrt{\frac{D}{\pi f}}$.

Because it is a function of the frequency of the periodic heat source, the thermal diffusion

length is used extensively to measure thermal properties of multi-layered samples.

Higher frequencies result in less penetration and smaller diffusion lengths while lower

frequencies are used for deeper thermal penetration and larger thermal diffusion lengths.

1.2   Nuclear Reactions and Nuclear Fuels

Nuclear energy is a very promising energy alternative to fossil fuels. Fission is

the main process by which nuclear energy is generated. The fission process releases a

very large amount of energy and heat which is then used to generate steam and drive

turbines. Nuclear fuel is extremely high in energy density. A single uranium fuel pellet

contains as much energy as 480 cubic meters of natural gas, 807 kilos of coal, or 149

gallons of oil. Nuclear reactors also have very high capacity factors, 90% or higher,

allowing them to run for months at a time without interruption. In addition, they produce

only a minor amount of greenhouse gases across the entire fuel cycle. It is just a small

fraction when compared to the greenhouse gases produced by traditional fossil fuel

methods. Approximately 20% of the total electricity generated in the US is produced by

nuclear energy [6].

Nuclear fuels are those that contain elements that are capable of nuclear fission,

with the most common being uranium-235 (^{235}U) or plutonium-239 (^{239}Pu). These are

isotopes with respective atomic masses of 235 and 239. In nuclear reactors, the fissile

materials absorb neutrons and split into the fission products. This process often produces

free neutrons, photons, and a large amount of energy. A portion of the free neutrons may

continue to interact with other fissile atoms and thus trigger nuclear chain reactions.

Control rods and neutron generators can be used to slow down or stop chain reactions if there are unsafe conditions in the reactor.

1.3 Cerium Oxide

While it would be ideal to measure irradiated nuclear fuel directly, working with radioactive materials presents many obvious difficulties. It is therefore much easier to measure a different, nonradioactive material with similar crystallography and thermal properties. Cerium Oxide (CeO_2) is a suitable and attractive substitute to Uranium Oxide (UO_2) when it comes to testing purposes. CeO_2 is a nonradioactive lanthanide oxide with fluorite microstructure, meaning it has the same structure as Calcium Fluoride. Neptunium, Plutonium and Uranium oxides have the same fluorite structure, but they are radioactive after they have been irradiated. Cerium Oxide has low solubility and high radiation stability. Because of its similar thermophysical properties and microstructure to UO_2, CeO_2 is an appropriate alternative to be used to measure the thermal boundary resistance of its grain interfaces. The values measured in this study will be comparable to those of UO_2 and other materials with like structure and properties.

1.4 Grain Boundaries

In polycrystalline materials, a grain boundary is an interfacial, two-dimensional defect or interface separating two grains or crystals having different crystallographic orientations. These boundaries probably measure the distance of only several atoms wide and represent an atomic mismatch when transitioning from the crystalline orientation of a grain to that of an adjacent one. It is important to note that not all boundaries are the

same and thus there exists a range of differing levels of atomic mismatch regions.

Boundaries vary in the extent of misorientation between two grains, or angle of

misalignment. They are typically classified as high-angle or small-angle based on the

degree of misorientation between two grains. A schematic of grain boundaries can be

seen in Figure 1.2.
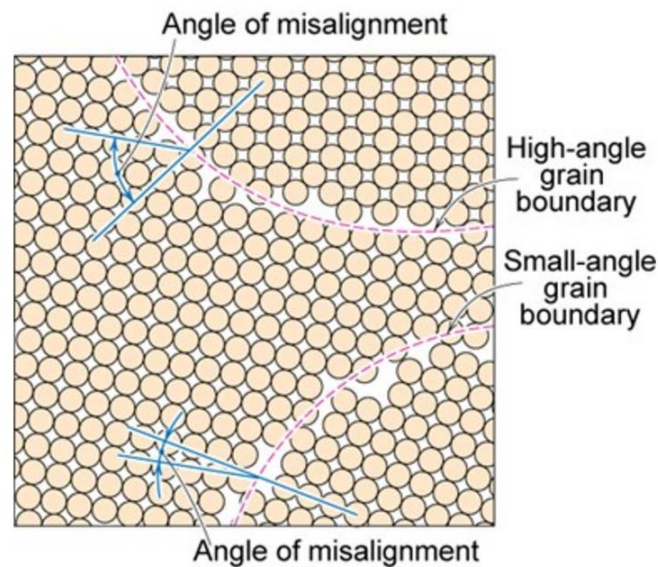
Figure 1.2: Schematic diagram showing atom positions at grain interfaces with high-
angle and small-angle grain boundaries [7].

Grain boundaries usually reduce the thermal and electrical conductivity of a

material. This effect increases in materials with smaller grains since there are then more

grain boundaries. Different grain boundaries most likely affect heat flow to different

degrees based on their angle of orientation and width. While it is not a focus of this

study, grain boundaries are also important factors when discussing the solid properties of

materials [7]. A micrograph of a polycrystalline metal displaying grain interfaces can be

seen in the following Figure 1.3.
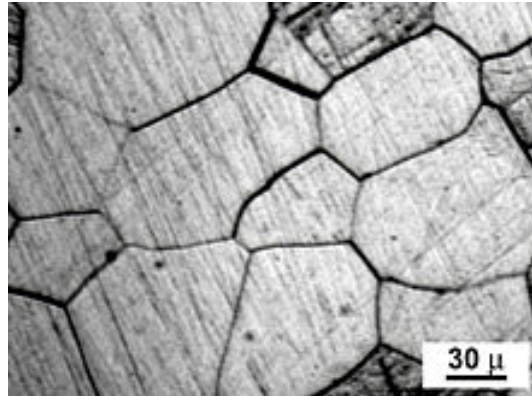
Figure 1.3: Micrograph of a polycrystalline metal [8].

1.5   Motivation

In non-metallic polycrystalline materials, the natural interfaces between grains

scatter energy carriers like phonons and thus reduce the overall thermal conductivity. An

improved understanding of the thermal transport process across grain boundaries can lead

to a better estimate of the thermal performance of a given polycrystalline material at both

the macro and micro scale. This is especially relevant in nuclear energy applications.

Better knowledge of how thermal energy interacts with grain boundaries can lead to

increased efficiency and safety of nuclear reactors.

The main purpose of this project is to characterize and quantify the thermal

resistance arising from grain boundaries of CeO_2 using a photothermal reflectance

measurement technique. The theory of this technique will be discussed in further detail

in Chapter 4. CeO_2 was chosen because it has many similar properties to UO_2.
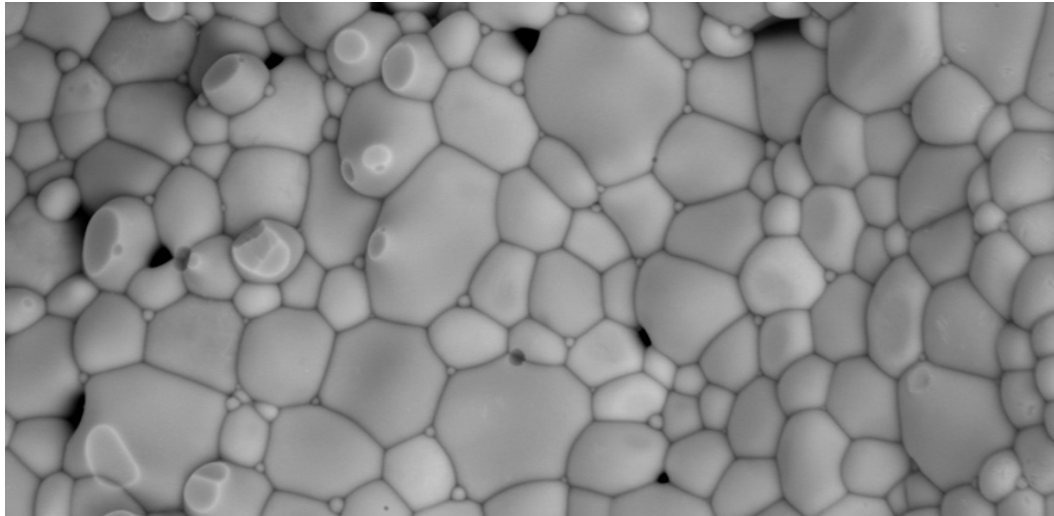
Figure 1.4: Magnified image of the microstructure of pure UO_2 simfuel [9].

1.6 Thesis Overview

This master's thesis is divided into four main parts. Chapters 2 – 4 contain a literature review, the objectives of the thesis project, and discuss the theory of the method used to measure the thermal resistance. The experimental details along with the sample description are discussed in Chapter 5. The results of the experiment and related discussion are in Chapters 6. Finally, Chapter 7 contains conclusions and a discussion on potential future work.

CHAPTER 2

LITERATURE REVIEW

In this chapter, relevant theoretical works which provide a broad background to this project are explored. They include a discussion on phonon transport, Cerium Oxide, grain boundary resistance in other materials, and different photothermal techniques for measuring thermal properties.

2.1   Grain Boundaries and Interfaces

Since the innovative work of Kapitza in 1941 [10], it has become common knowledge that there exists a temperature discontinuity at the interface between different materials due to the presence of a thermal interface resistance. Kapitza was the first to observe the thermal interface behavior in a liquid helium/solid interface. The term "Kapitza resistance" was initially used to only describe the thermal resistance of solid/liquid interfaces at cryogenic temperatures, such as liquid helium and copper. However, it is now commonly used to describe the thermal resistance of solid/solid interfaces of differing materials as well as those of the same material, like naturally occurring grains. While the thermal boundary resistance between two different materials has been studied extensively, the thermal resistance across grain boundaries of the same material has not been widely explored.

For nonmetallic crystalline solids at low and medium temperatures, heat is conducted by lattice vibrations, or phonons. Grain boundaries decrease the overall thermal conductivity by scattering the phonons. This act of scattering is done in multiple ways. In a crystal structure with anisotropic properties, there is a change of grain

orientation across the interface which results in a change in the velocity of vibrational propagation in the direction of the heat flow. The other method by which grain interfaces interfere with lattice vibration is due to the fact that the grain boundary represents a disordered region which also results in local change in phonon velocity. The latter method has been determined to be the more significant mode of interference [11,12]. Grain boundaries also reduce the overall thermal conductivity of a polycrystalline because the phonon mean free path is limited by the size of grains. Thus, smaller grains result in lower overall thermal conductivity of a material because of a smaller mean path.

Several models have been developed to explore the influence of atomic structure on phonon transport across boundaries [13,14]. Two of the more popular ones are the acoustic mismatch model (AMM) and the diffusive mismatch model (DMM). Both of these models are elastic, or specify that a phonon with a particular frequency can only generate another phonon on the opposite side of the interface with that same frequency. For the DMM, the phonon has no prior memory of where it came from after it arrives at the interface and will scatter diffusively. The opposite is true of the AMM. Phonons are transmitted through the interface or reflected based on the incident angle at the boundary. Many times, the AMM and the DMM create an upper and lower limit where the actual measured Kapitza resistance is somewhere in between [4]. These models require validation by carrying out experimental measurements and investigating the phonon transport process across individual, well defined grain boundaries.

2.1.1 Grain-Size Effects

As stated previously, the average size of grains contributes greatly to the thermal conductivity of a material. Its effect can be derived from the concept that the grain boundaries are thermal resistors in series with the grains. This results in in the following equation [2]:

$$k = \frac{k_i}{1 + \frac{R_k k_i}{d}} \tag{2.1}$$

Where k_i is the intrinsic conductivity or the thermal conductivity of a single crystal, d is the average grain size, and R_k is the thermal boundary resistance.

Another term that is useful when investigating the effect of grain size on thermal conductivity of polycrystalline materials is the Kapitza length l_k. It is defined as the thickness of the material of thermal conductivity k that provides the same change in temperature as a given boundary [15]. It is given in the following form:

$$l_k = \frac{k}{G_k} \tag{2.2}$$

Where G_k is the Kapitza conductance. If the grain size is significantly larger than the Kapitza length, $d > l_k$, then the grain size effect on the thermal conductivity of the material should be minor. However, as the size of the grains approaches the Kapitza length, the phonon scattering at the interface becomes significant and will reduce the thermal conductivity compared to the same material with larger grains.

It is interesting to note that for some materials the influence of the grain size on the thermal conductivity decreases with increasing temperature. At the very highest of temperatures, the grain size has little to no effect on the overall thermal conductivity.

Smaller grains do not result in lower values of total thermal conductivity at very high

temperatures when compared to the same material with bigger grains [2,16]. This can be

seen in the following Figure 2.1.
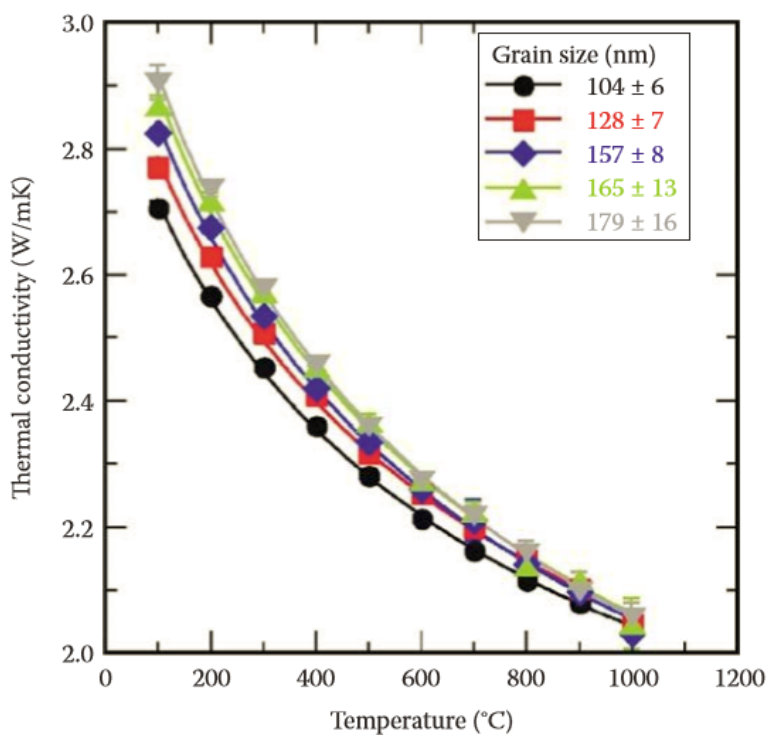
Figure 2.1: Thermal conductivity as a function of temperature for tetragonal zirconia
stabilized at different grain sizes [16].

2.2   Cerium Oxide Studies

Cerium Oxide is a popular material that has been investigated extensively due to

its similarities to UO_2. Studies have been carried out to measure physical, chemical, and

electrochemical properties as well as crystal structure, atomic structure, and

thermophysical properties [17–20]. While the average Kapitza conductance and other

thermal properties have been researched in a few studies [20,21], the thermal resistance

of individual grain boundaries is a topic that has yet to be explored in great detail,
especially as it relates to grain boundary angles.

The crystal structure of Cerium Oxide is the same as Calcium Fluoride. This cubic
crystal structure is referred to as fluorite. It maintains this structure at all temperatures up
to its melting point. The microstructure of Cerium Oxide can be seen in Figure 2.2.
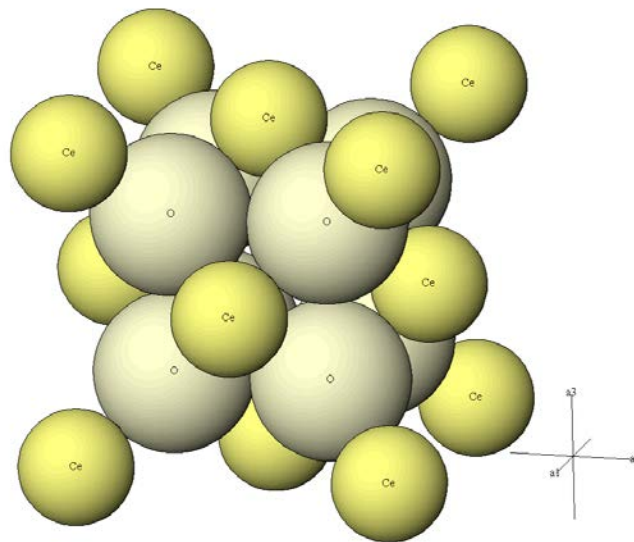
Figure 2.2: Microstructure of Cerium Oxide [22].

2.2.1 Cerium Oxide Thermal Conductivity and Kapitza Conductivity

Of particular interest to this thesis project are the studies that explored the thermal
properties of CeO_2. One study by Khafizov *et al.* measured the thermal conductivity in
nanocrystalline ceria thin films using a laser-based modulated thermoreflectance
technique [21]. The purpose of this study was to characterize the influence that point
defects, dislocations, and grain boundaries have in limiting heat flow. Khafizov *et al.*

determined that the film's measured thermal conductivity was significantly less when compared to stoichiometric bulk CeO_2. Using multiple microstructure techniques, it was determined from this study that thermal conductivity was influenced by grain boundaries, dislocations, and oxygen vacancies.

Khafizov *et al.* first performed thermal transport measurements on a large grained (average grain size ~ 5 microns), stoichiometric, CeO_2 polycrystalline pellet. The thermal diffusivity was measured using the laser flash method and the resulting thermal conductivity was then calculated using Equation 1.3. Results for the measured thermal diffusivity and conductivity over a broad temperature range can be seen in Figure 2.3 and Figure 2.4, respectively.
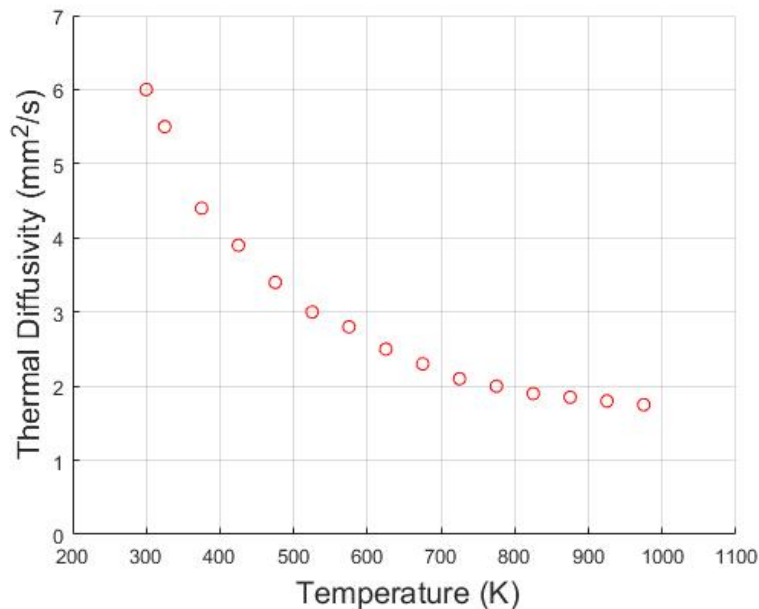
Figure 2.3: Thermal diffusivity of CeO_2 pellet using laser flash apparatus [21].
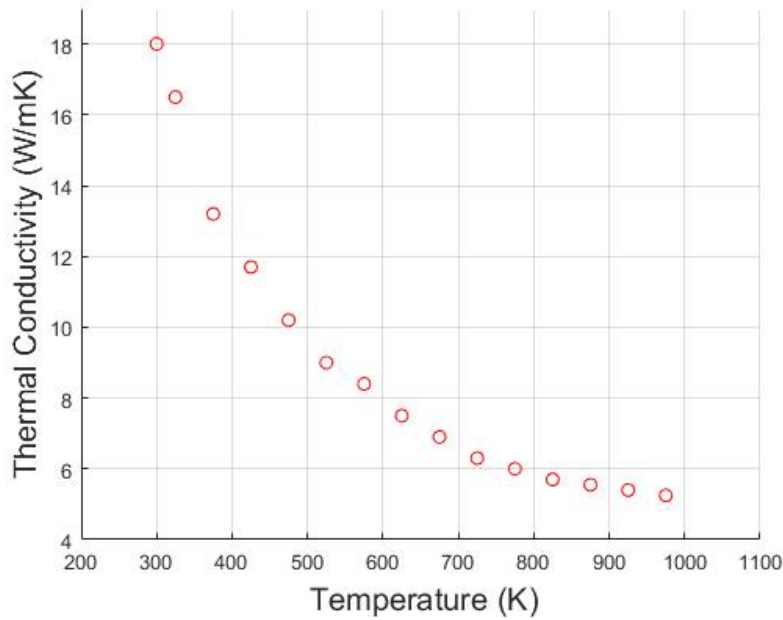
Figure 2.4: Corresponding thermal conductivity [21].

A method developed by Nan and Birringer [15], also known as the effective medium method, was then used to determine the average Kapitza conductance by using the overall thermal conductivity and the intrinsic conductivity of the material in the grains. The expression is as follows:

$$\frac{1}{k} = \frac{1}{k_i} + \frac{1}{G_k d}$$

(2.3)

This is a rewritten version of Equation 2.1 while also replacing the Kapitza resistance with its inverse, or Kapitza conductance. The temperature dependence of G_k can be expressed by the following

$$G_k(T) = \frac{k_B}{2\pi^2 v^2} \int_0^{\omega_D} C(T, \omega) \alpha(\omega) \omega^2 d\omega$$

(2.4)

where $\alpha(\omega)$ is the frequency dependent transmission coefficient.

Measured results from this study of the thin film of ceria can be found in the following figures. Figure 2.5 represents the measured thermal wave phase profile as a function of probe scan distance, where the heating pump laser is at the origin. The theory of using the phase profile to determine thermal properties will be discussed in further detail in Chapter 4. Figure 2.6 is the measured inverse thermal conductivity in grains as a function of the inverse of the grain size.
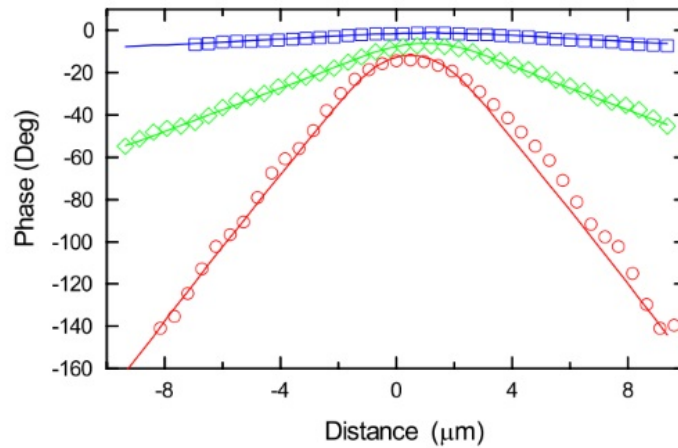
Figure 2.5: Thermal wave profile in ceria thin film at 3 different modulated frequencies with fitted lines. Pump laser is at the origin [21].
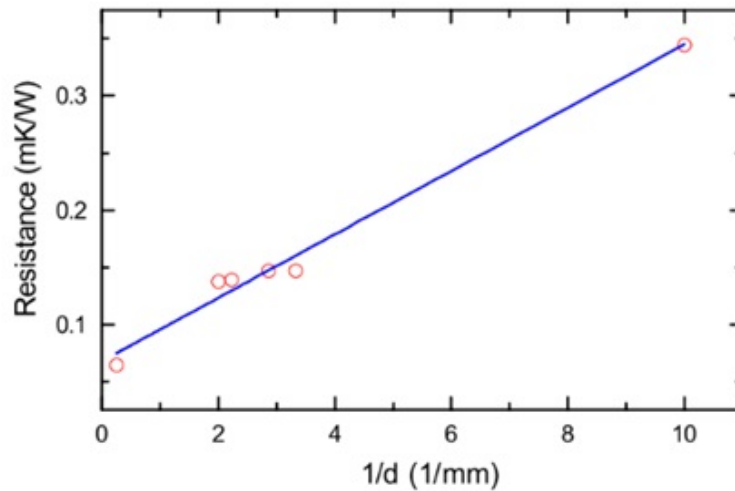
Figure 2.6: Dependence of thermal conductivity on grain size at room temperature measured using modulated thermoreflectance microscopy [21].

By using the overall conductivity and intrinsic thermal conductivity, Khafizov *et al.* were able to determine a best fit value for the average Kapitza conductance, which is $G_k = 0.036\ GW/m^2K$. No previous values had been reported so they were unable to validate their results with any other experimental values. However, Molecular dynamics (MD) simulations were also performed to prove the validity of the measured value. Different types of grain boundaries were considered in the simulations. The results for the boundary conductance can be seen in the following Table 2.1.

Table 2.1: Kapitza conductance of different grain boundary orientations in CeO_2 calculated by MD [21]**.**

Grain-boundary type	Boundary conductance (GW/m^2K)
Σ3	2.3
Σ11	2.7
Σ13	3.3
Σ3 ($UO_2\ at\ 800K$)	1.6

It can clearly be seen from the preceding table that the values based on MD simulations are considerably higher when compared to the experimental result. The conclusion is that the boundary conductance measured is anomalously small compared with ideal boundaries. The results of this study will be examined again when compared to the results of this thesis study in Chapter 6.

2.2.2   Thermophysical Properties of CeO₂ Compared to UO₂ and PuO₂

Another study with a lot of relevance to this project was done by Nelson *et al.*
[20]. In it, they measure the thermal conductivity, thermal diffusivity, and other thermal
properties of CeO₂ over a wide temperature range. The main objective of the study was
to compare measured thermal values of CeO₂ to those of known values of UO₂ and PuO₂
to determine its suitability as a substitute in nuclear fuel applications where heat transfer
is the primary concern for performance. Extra care was implemented in order to maintain
the stoichiometry of the sample because of its importance to thermal transport properties.
Results for measured values compared to UO₂ and PuO₂ can be seen in the following
graphs.
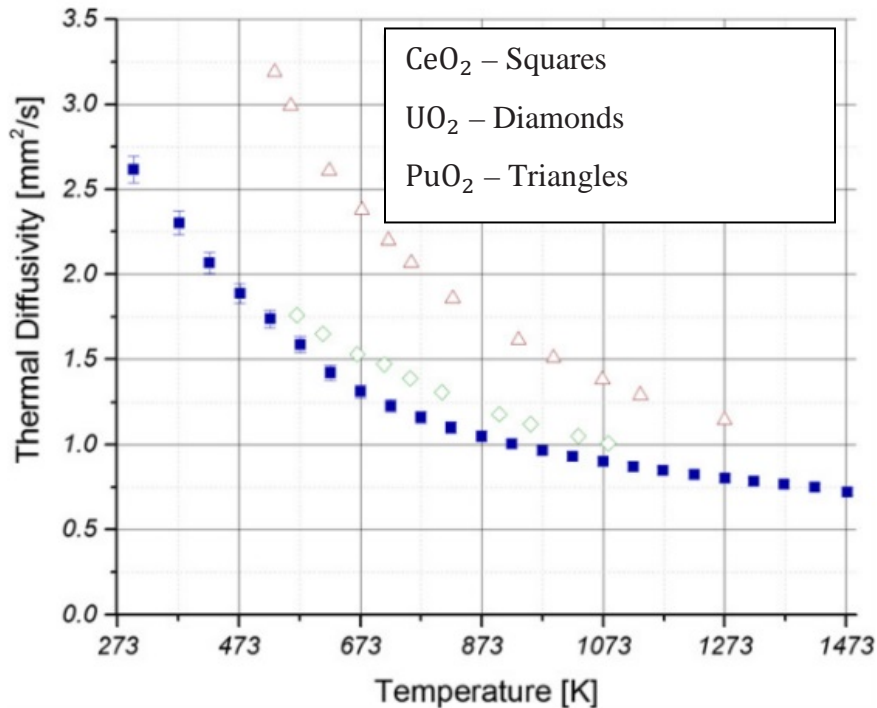
Figure 2.7: Thermal diffusivity of CeO₂, UO₂, and PuO₂ over a wide temperature
range [20].
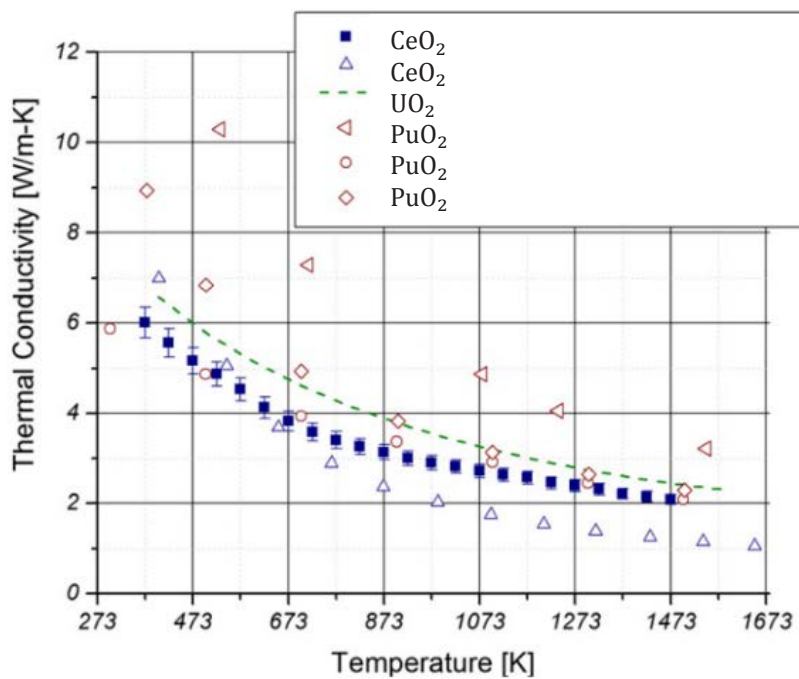
Figure 2.8: Thermal conductivity of CeO_2, UO_2, and PuO_2 over a wide temperature range [20].
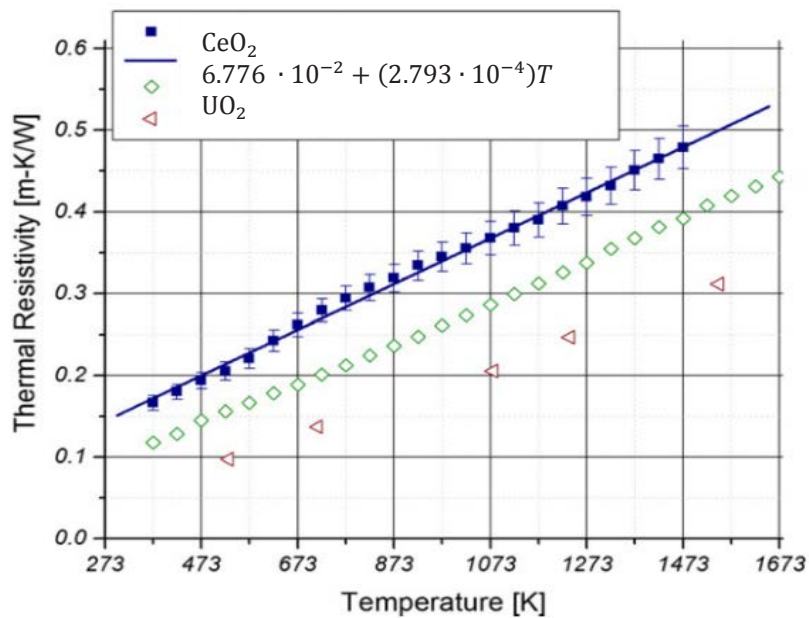
Figure 2.9: Thermal resistivity of CeO_2, UO_2, and PuO_2 over a wide temperature range [20].

While they are not included, graphs of thermal expansion and specific heat capacity were also plotted and compared to literature values of UO_2 and PuO_2. The measured values of thermal expansion and specific heat for CeO_2 agree well with literature values of UO_2 and PuO_2. Although Nelson *et al.* were unable to find published data for the CeO_2 thermal diffusivity, Khafizov *et al.* [21] measured the diffusivity of a pellet of CeO_2 over a wide thermal range and the results are recorded in Figure 7. There is a small discrepancy between the two studies, with the latter measuring a value for the diffusivity and conductivity that was approximately three times larger than the former. Nelson *et al.* concluded that all of the measured thermophysical properties of CeO_2 in their study had portrayed significant differences compared to those of PuO_2, but that the thermal conductivity of CeO_2 and UO_2 is generally comparable below 1673 K. This last conclusion is important to this thesis and a driving motivator to study CeO_2 since its thermal transport properties are comparable to those of UO_2.

2.3   Grain Boundary Resistance in Other Materials

While CeO_2 is the main material of interest in this study, it has received relatively little attention concerning its interfacial thermal resistance. However, this is a topic that has been explored in other materials and is discussed in this section.

In one study, Smith *et al.* [11] researched the influence of grain boundaries on heat transport of sintered polycrystalline alumina over a broad temperature range. Both small-grained porous ceramics and large-grained dense ceramics were studied using the laser-flash technique, and multiple methods were used in order to determine the average Kapitza resistance of the grain boundaries. It is also important to note that alumina

ceramics with significant differences in microstructure were studied. Like previous

studies, the thermal conductivity was evaluated by first measuring the thermal diffusivity

and then calculating the conductivity.

One of the conclusions made by Smith *et al.* is that if a ceramic material is more

porous, it will have an increase in the thermal resistivity of its grains and the equivalent

grain-boundary resistance. This can be seen in the following Figure 2.10 and Table 2.2.
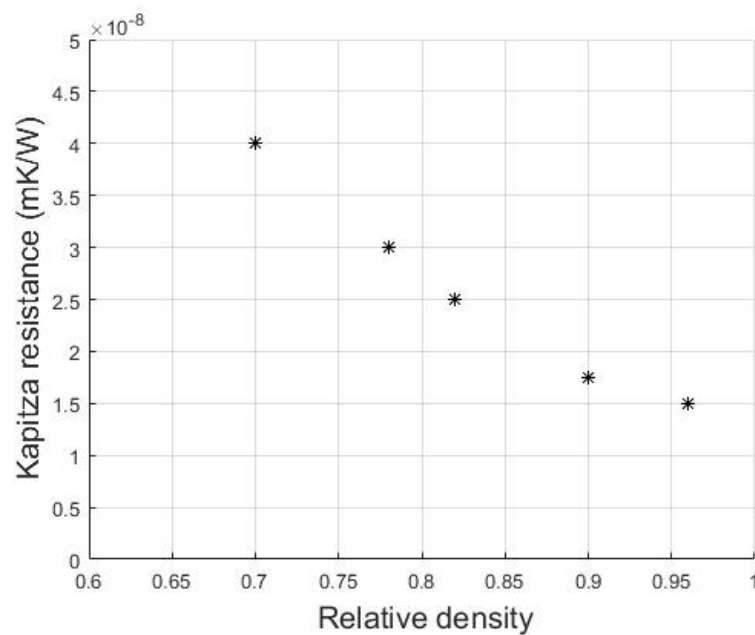
Figure 2.10: Kapitza resistance of grain boundaries in alumina as a function of
relative density [10].

Table 2.2: Interfacial Resistance in dense alumina ceramics [11]**.**

Relative density	Measured R_k $(m^2 \cdot K/W)$
0.70	$4.1 \cdot 10^{-8}$
0.76	$3.0 \cdot 10^{-8}$
0.82	$2.5 \cdot 10^{-8}$
0.9	$1.6 \cdot 10^{-8}$
0.96	$1.5 \cdot 10^{-8}$

The results from this study confirm that there is a direct correlation between the porosity of the solid and the grain boundary resistance. Dense, large grained ceramics have a lower average grain boundary thermal resistance when compared to porous, small grained ceramics. The larger resistance in more porous media is due a decrease in the effective heat conducting cross section and the generally smaller grain size.

The average Kapitza resistance measured by Smith *et al.* in dense alumina was found to be ~$1.3 \cdot 10^{-8} \ m^2 \cdot K/W$. In alumina containing a pore volume fraction of 0.3, the thermal resistance across grain boundaries was $2.2 \cdot 10^{-8} \ m^2 \cdot K/W$. Smith *et al.* also suggested, based on research and literature, that a typical value for the thermal resistance across grain boundaries is in the range of $10^{-8} - 10^{-7} \ m^2 \cdot K/W$. While it is not expected that all materials have identical values of thermal boundary resistance, measuring a value of the Kapitza resistance for CeO_2 that is relatively close to this range would provide more confidence in the measured results of this thesis experiment.

Another study done by Yang *et al.* [23] sought to characterize the Kapitza resistance of nanocrystalline yttria-stabilized zirconia. This study focused on the

nanoscale and therefore the grain boundaries played a larger role in affecting the overall

heat transfer because the fraction of atoms located in close proximity to one or more

interfaces becomes significant. Yang *et al.* used multiple methods and the use of the

effective medium method in determining the Kapitza resistance for their sample. In their

method, the multi-grain sample is assumed to consist of perfect crystal grains, all of

which have the same thermal properties. Some of their results are as follows:
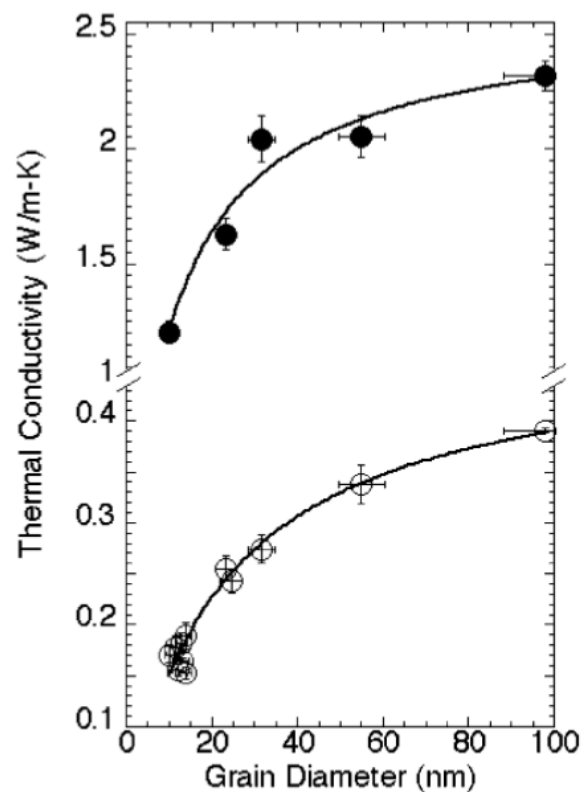
Figure 2.11: Thermal conductivity as a function of grain size of yttria-
stabilized zirconia [23].
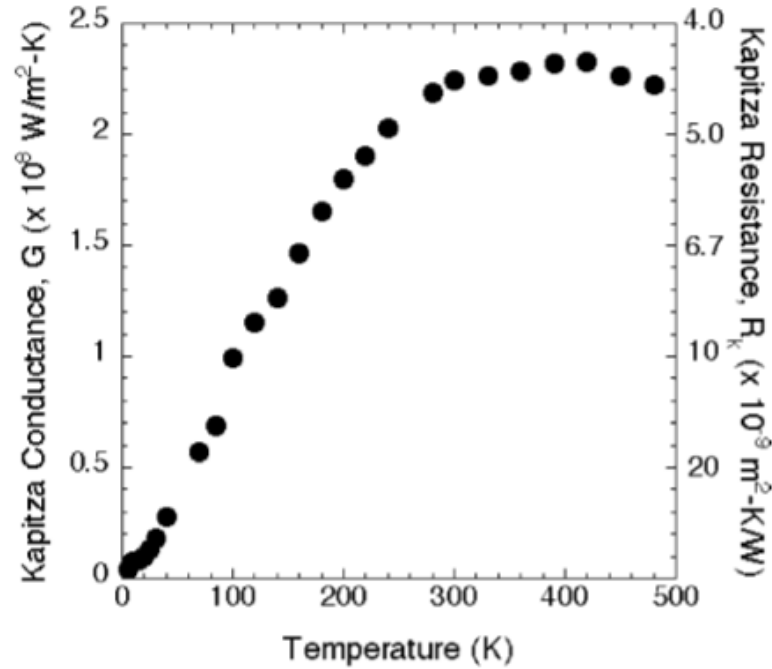
Figure 2.12: Kapitza conductivity and resistance as a function of temperature of yttria-stabilized zirconia [23].

The measured result of Kapitza resistance is of most interest. At room temperature this value is approximately $4.5 \cdot 10^{-9} \, m^2 \cdot K \cdot W^{-1}$. This is smaller than the range of $10^{-8} - 10^{-7} \, m^2 \cdot K \cdot W^{-1}$ proposed by Smith *et al.* [11], but as mentioned before, that range cannot be expected for every single material.

Another literature study that explored the Kapitza resistance of a material is that of Hurley *et al.* [24]. In it, they measure the thermal resistance across a Si/ SiO$_2$ interface using a time resolved thermal wave microscopy technique. This study is particular relevant because it incorporates much of the same theory that is used in this thesis. Parts of this study will be discussed in further detail in Chapter 5. The final weighted average value for the thermal resistance across the grain boundaries was $2.3 \cdot 10^{-9} \, m^2 \cdot K \cdot$

W^{-1}. It was compared to analytical models for Si/ SiO$_2$ Kapitza resistance done in other studies. Hu *et al.* [25] anticipated a value of $2.4 \cdot 10^{-9} \, m^2 \cdot K \cdot W^{-1}$ using the AMM and $3.5 \cdot 10^{-9} \, m^2 \cdot K \cdot W^{-1}$ using the DMM. The value obtained from the AMM more closely matched the measured value from Hurley *et al.*

An additional study to be discussed that investigates the thermal resistance across grain boundaries is the one done by Watanabe *et al.* [26]. In this study, MD simulations are used to quantify the Kapitza resistance of UO$_2$, which is of particular interest to this thesis study. Using two different models that each incorporated the effective medium method, Watanabe *et al.* [26] generated the results seen in Figure 2.13. At room temperature, the Kapitza conductance was determined to be approximately $0.15 \, GW/m^2 K$ from one model and approximately $0.3 \, GW/m^2 K$ from the other. The results of this study will be discussed in further detail when compared to the measured results of CeO$_2$ in Chapter 6.
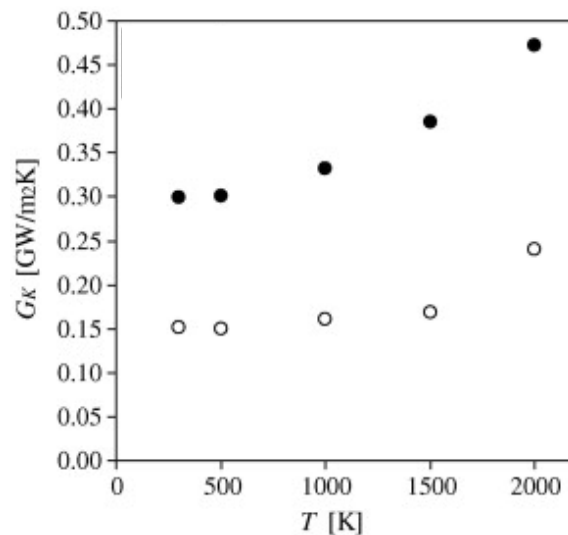
Figure 2.13: Kapitza conductance of grain boundaries from polycrystalline UO$_2$ MD simulations. Two models are shown [26].

2.4   Thermal Transport Measurement Techniques

In this section, different measurement methods are discussed. Photothermal techniques in particular are reviewed as they are among the most popular transient techniques to measure thermal transport properties with high spatial resolution. It is the spatial-scan photothermal reflectance technique that is used in this study to measure the thermal resistance across grain interfaces of CeO_2.

2.4.1   Traditional Measurements of Thermal Properties

Before the discovery and implementation of thermal reflectance techniques to study thermal properties of materials, many other approaches were used. Standard methods for measuring thermal conductivity, for example, involve applying a heat flux across a material of a known geometry and then measuring the temperature difference across a set distance, usually with the aid of thermocouples. Using Fourier's law, the thermal conductivity can then be calculated. This method also requires that the temperature of whatever is being measured reach a steady state and generally requires centimeter-size samples or larger. Besides the size of the sample and steady state requirements, there are also a few other drawbacks and considerations to take into account with this method. There is the thermal contact resistance between the thermocouple and sample that needs to be factored in. Also, this method is impractical for high-temperature measurements because of the unavailability of high-temperature thermocouples and large radiative heat losses through the surface of the sample.

The opposite of steady-state measurements, or transient methods, are those that measure time-dependent temperature responses to a heat input in order to determine

thermal properties based on the transient heat conduction equation. The heat source can also be periodic or short in its duration. Current photothermal techniques are examples of transient methods.

Although analytical solutions for transient methods are more complicated than those for steady-state methods, they have a few advantages. When given a well-defined heat source and proper boundary conditions, more thermal properties can be obtained from non-steady-state methods with good spatial accuracy. Photothermal techniques that are laser-based also have the added benefits that the measurements are non-contact and non-destructive. Micrometer spatial resolution is possible with proper laser selection and modulation, which is necessary for this study.

2.4.2   Photothermal Techniques

Due to their well-defined optical coupling conditions, experimental techniques which use lasers to generate and detect heat pulses have gained in popularity for making accurate thermal transport measurements [27]. Some examples of popular photothermal techniques are detailed in this section.

The photoacoustic technique involves acoustically detecting the thermal expansion of a sample generated by sound waves. Harmonic thermal expansion and contraction of the sample surface due to localized heating causes the surrounding gas layer to expand and compress periodically. This periodic thermal expansion generates a pressure wave or detectable acoustic signal that can ultimately be used to identify the absorbing components of the sample. The development of the laser, as well as the use of

microphones and lock-in amplifiers, has made this a popular and effective method to measure thermal properties [28].

The laser flash method is another popular laser based method. It is implemented on a disk shaped sample with flat parallel surfaces, much like the one in Figure 2.14. One side of the specimen is heated by a short laser pulse while the infrared emission is measured on the opposite side. The time that it takes for the other side to be heated is used to determine the thermal conductivity of the material. It is a bulk measurement technique in that it provides an averaged value across the thickness of the sample [29].

Temperature Signal
versus Time

Laser Pulse
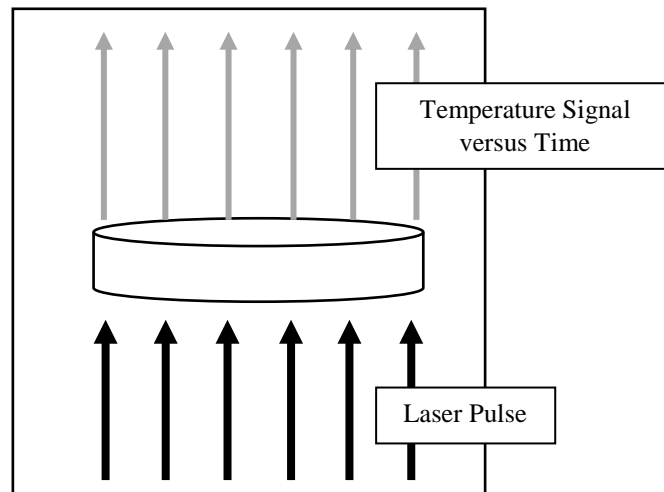
Figure 2.14: Laser Flash Technique.

The Photothermal displacement spectroscopy method is another technique which uses a modulated pump laser beam to generate a regional temperature fluctuation and thermoelastic deformation on the sample surface, which is then detected by the variation of the reflection angle of an incident probe laser beam. By analyzing the variation of the reflection angle in the frequency domain or time domain, the sample optical absorption,

thermal expansion coefficient, thermal diffusion length and thermal conductivity can be determined [30].
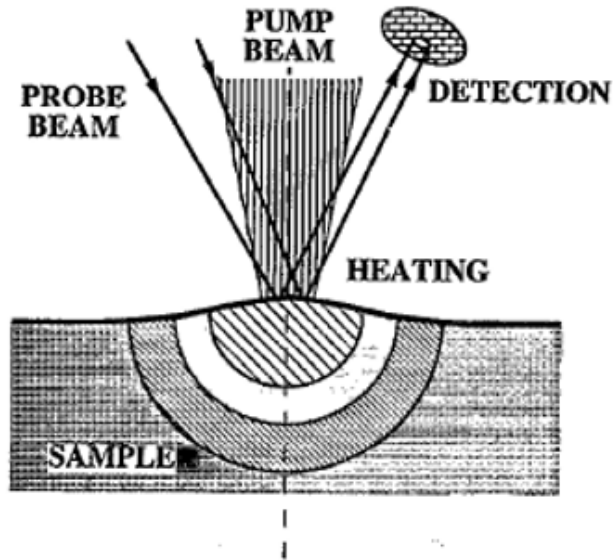
Figure 2.15: Representation of the photothermal displacement technique with thermophysical deformation caused from the heating [31].

The photothermal deflection technique is another well-established photothermal method. By way of this technique, the refractive index gradient that is related to the temperature gradient of the surrounding gas on the heated surface is observed. This is also sometimes referred to as detection by the "mirage effect." A schematic of a typical setup can be seen in Figure 2.16. A heating laser is used to generate a thermal wave on the surface of the sample. A probe laser is then used to detect the refractive index gradient by passing though the heated gas while a position-sensing detector monitors the probe beam deflection [32].
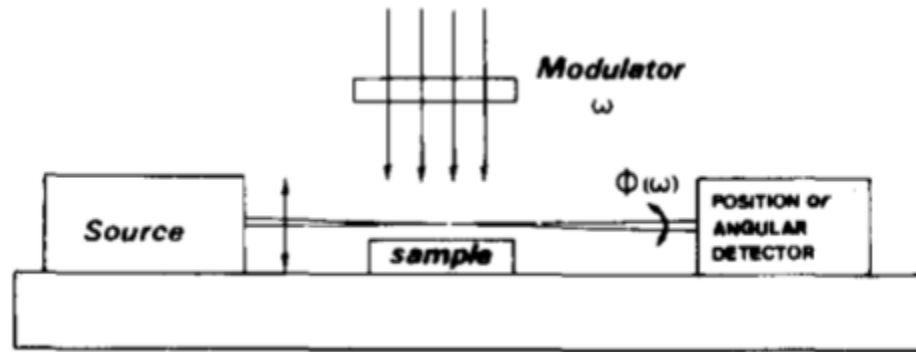
Figure 2.16: Typical experimental setup of the photothermal deflection technique [32].

The last technique to be discussed and the one that is used in this study is the photothermal reflectance technique. The change of the optical reflectivity of a material is a linear function of the temperature change if this change is no more than a few tens to a hundred degrees. The rate of optical reflectivity change is defined as the temperature coefficient of optical reflectivity. Properties such as thermal diffusivity, effusivity and conductivity can be measured using this technique.

Samples and materials used in these laser based methods are typically coated with thin metallic layers in order to increase the thermal absorption and thermoreflectance effect. Depending on the application, laser excitation for photothermal techniques can be implemented in the time domain [33,34], frequency domain [35], spatial domain [36,37], or a hybrid technique composed of multiple domains [24,38]. Time domain methods involve using pulsed lasers while frequency and spatial domain methods use continuous-wave lasers. Frequency domain methods alter the frequency of the heating laser while spatial domain methods vary the separation distance between the heating laser and the probe laser. Frequency and spatial domain measurements are often used to investigate

thermal transport in the lateral direction. This generally allows for easier measurements of target interfaces found in bulk structures that intersect the surface of the sample. Examples of different typical phase profiles generated in frequency and spatial domains can be seen in the following figures.
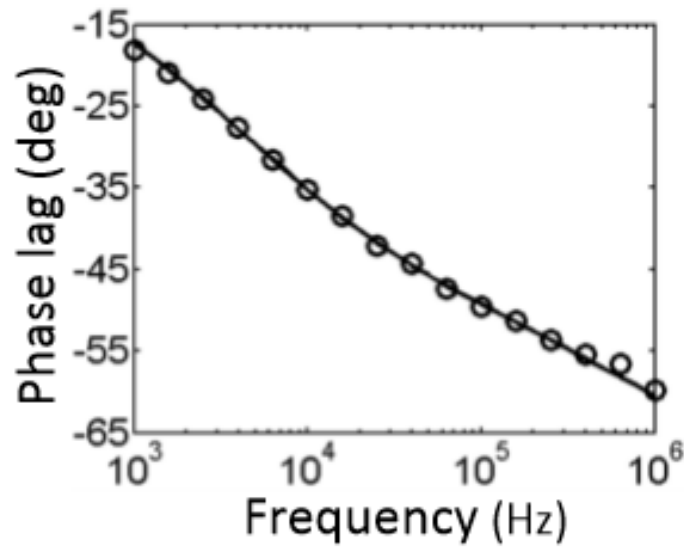
Figure 2.17: Phase profile in the frequency domain [38].
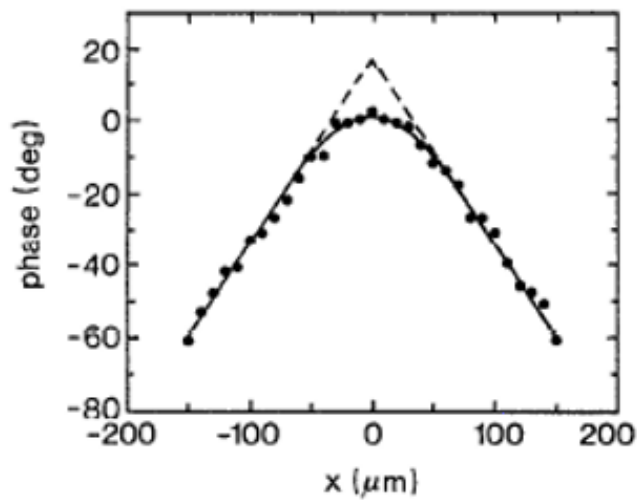
Figure 2.18: Typical phase profile in the spatial domain [39].

Figure 2.19 is a representation of how a phase diagram with a phase shift can be used to find the thermal resistance of an interface.
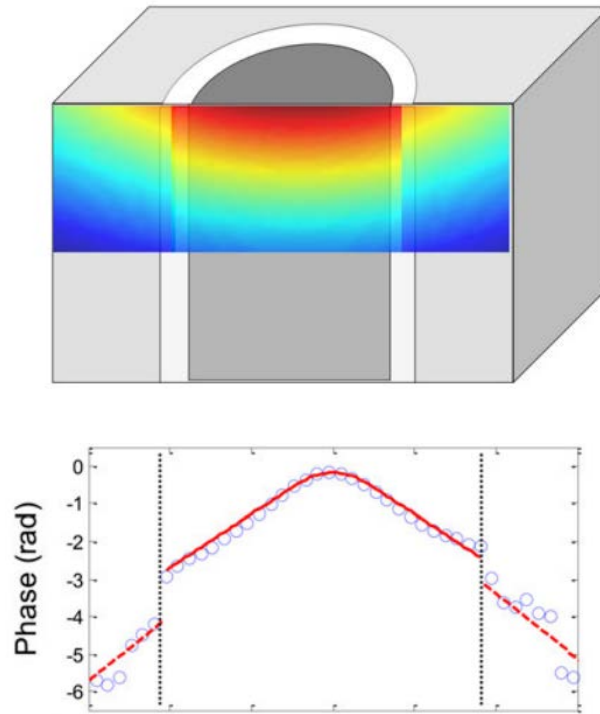
Figure 2.19: Spatially resolved thermal transport in a composite fiber with the resulting phase profile and phase shifts [40].

2.5   Conclusion of Literature Review

The method used and discussed in this study to measure the resistance across crystallite interfaces is the spatial-scan photothermal reflectance technique. Traditional measurement methods, such as the laser flash technique or contact methods, are ultimately insufficient when it comes to accurately measuring the Kapitza resistance. The thermal resistance of grain boundaries is usually very small (on the magnitude of $10^{-8} m^2 \cdot K/W$ or less). In traditional contact methods, the contact thermal resistance between the sample and invasive probes (such as thermocouples) would be too dominating. This dominance would overshadow the smaller Kapitza resistance of the

sample and ultimately produce significant errors in the results. Traditional measurement techniques may also have difficulties precisely locating a suitable target boundary since the grains are very small, measuring only a few micrometers in diameter. The SSPRT is capable of high spatial resolution on the micro scale and has the added benefits that the measurements are non-contact and non-destructive as long as the laser power is not set too high, thus allowing for multiple measurements. It is the method used in this study to measure the Kapitza resistance of crystalline interfaces. The theory behind this method is discussed in further detail in Chapter 4.

CHAPTER 3

OBJECTIVES

The main goal of this work is to investigate and quantify the thermal resistance generated by the presence of grain interfaces in CeO_2 and to validate the results by comparing them to values found in other studies. This will be carried out using the spatial-scan photothermal reflectance technique. The specific steps and objectives include:

- Obtain a suitable sample of Cerium Oxide and identify multiple target grain boundaries (50-80).

- Measure the phase lag vs laser separation distance using the spatial-scan photothermal reflectance technique at the target locations and extract the Kapitza resistance using a multi-parameter fitting process.

- Perform a statistical analysis of the measured data and validate the results by comparing them to other measurements found in literature.

- Discuss results, conclusions, and future work.

CHAPTER 4

METHOD THEORY

In this chapter, the theoretical details of the measurement process are discussed. The spatial-scan photothermal reflectance technique is the method of choice for this study and its theory will be explored. It is considered an ideal method for grain interface measurements due to the non-contact, non-destructive features and micrometer spatial resolution. The principle of the spatial-scan photothermal reflectance technique involves heating the sample with an intensity-modulated laser and scanning another constant intensity laser across the surface to detect the thermal wave propagation by optical reflectance. The phase lag versus laser separation distance relation can be used to extract the thermal diffusivity of a sample in a straight forward manner. When the thermal wave encounters a grain boundary, a phase shift is generated. A fitting process can then be used to determine the thermal resistance from the phase profile. Photothermal techniques have been successful in measuring localized thermal properties on a microscale [35] and quantifying the thermal resistance across interfaces of other materials [24,41].

4.1 Spatial-Scan Photothermal Reflectance Technique

The following is the physical science behind the photothermal technique. The model and coordinate system for the derivation are shown in Figure 4.1. The three-dimensional heat equation for isotropic thermal conductivity is as follows.

$$\frac{\partial^2 T}{\partial x^2} + \frac{\partial^2 T}{\partial y^2} + \frac{\partial^2 T}{\partial z^2} + \frac{\dot{g}}{k} = \frac{1}{D}\frac{\partial T}{\partial t} \tag{4.1}$$
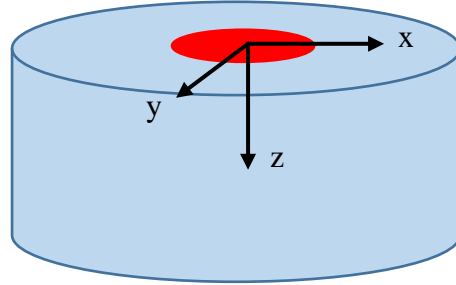
Figure 4.1: Coordinate system for the SSPRT.

First, let us consider an isotropic semi-infinite solid whose surface is heated uniformly by a harmonic heat source, which takes the form of $(P_0/2)[1 + \cos(\omega t)]$, where P_0 is the heat source intensity, $\omega = 2\pi f$ is the angular modulation frequency of the source, and t is the time. If the heated surface occupies the y-x plane and $z = 0$, and there is no heat generation in the sample, the temperature $T(z,t)$ distribution within the medium can be determined by solving the homogeneous one-dimensional heat diffusion equation:

$$\frac{\partial^2 T}{\partial z^2} - \frac{1}{D}\frac{\partial T}{\partial t} = 0 \quad z < 0, t > 0 \tag{4.2}$$

The boundary condition is as follows:

$$-k\frac{\partial T}{\partial z} = \frac{P_0}{2}[1 + \cos(\omega t)] = Re\left(\frac{P_0}{2}[1 + \exp(i\omega t)]\right) z = 0, t > 0 \tag{4.3}$$

which expresses that the periodic thermal energy applied at the surface of the solid is dissipated into its bulk by its conduction. Re stands for 'the real part of.'

The heating component is divided into two parts, $P_0/2$ and $(P_0/2)\exp(i\omega t)$, which respectively produce a dc temperature increase and an ac thermal modulation. The

dc component will be neglected since the ac component is of primary interest. In order to

solve Equation 4.2, it is assumed the periodic component has a solution of the form:

$$T(z,t) = Re(T(z)\exp(i\omega t)) \tag{4.4}$$

Omitting the 'Re' symbol and inserting the assumed solution into the general one-

dimensional heat equation gives the following:

$$e^{i\omega t}\left(\frac{d^2 T(z)}{dz^2} - \frac{i\omega}{D}T(z)\right) = 0 \tag{4.5}$$

Discarding the exponential time factor, the general solution for the spatial dependence of

the temperature may be expressed as:

$$T(z) = A\exp(-\phi z) + B\exp(\phi z), \qquad \phi = (1+i)\sqrt{\frac{\omega}{2D}} \tag{4.6}$$

where *A* and *B* are arbitrary constants. In order for *T(z)* to remain finite, the constant *B*

must be equal to zero. Otherwise, as *x* tends to infinity, *T(z)* will also go to infinity. *A* is

evaluated by applying the flux continuity boundary condition at the sample surface, $z = 0$.

$$\frac{P_0}{2} = -k\frac{\partial T(z)}{\partial(z)} = (-k)(-\phi)A\exp(-\phi z) \tag{4.7}$$

From which *A* is found to be $P_0/2k\phi$. The full solution is as follows:

$$T(z,t) = \frac{P_0}{2k\phi}\exp(-\phi z + i\omega t) \tag{4.8}$$

Or

$$T(z,t) = \frac{P_0}{2\sqrt{\rho c k \omega}} \exp\left(-z\sqrt{\frac{\omega}{2D}}\right) expi\left(\omega t - z\sqrt{\frac{\omega}{2D}} - \frac{\pi}{4}\right) \qquad (4.9)$$

Like normal propagating waves, the thermal wave has an oscillatory spatial dependence, with a wave vector given in the form of:

$$Re(\phi) = \frac{1}{L_{th}} = \sqrt{\frac{\omega}{2D}} \qquad (4.10)$$

in which the variable L_{th}, referred to as the thermal diffusion length, is defined as $\sqrt{(2D/\omega)}$. Accordingly, Equation 4.9 then becomes [42]:

$$T(z,t) = \frac{P_0}{2\sqrt{\rho c k \omega}} \exp(-z/L_{th}) \, expi\left(\omega t - z/L_{th} - \frac{\pi}{4}\right) \qquad (4.11)$$

The optical reflectivity of a material is known to be a linear function of its temperature if the temperature change is no more than a few degrees [43,31,38]. After inducing a periodic temperature variation on the surface of the sample, a probe laser can be used to detect this temperature change by means of the sample reflectance. The relative change of the sample reflectance $\Delta R/R$ due to the temperature change ΔT is expressed by the following:

$$\frac{\Delta R}{R} = \frac{1}{R}\frac{dR}{dT}\Delta T \qquad (4.12)$$

Knowing this, the surface of a sample can be heated using a laser beam with a periodically modulated intensity. The local optical reflectivity change (as an indicator of the temperature change) can then be measured from another laser beam with an unmodulated constant intensity. When compared to the heat source, the local

temperature change has the same frequency with a phase difference. This phase

difference can be used to extract the thermal properties of the sample material. Figure

4.2 is a schematic of the two lasers interacting with the sample surface. The heating laser

remains stationary while the probe laser scans across the sample in the x direction.
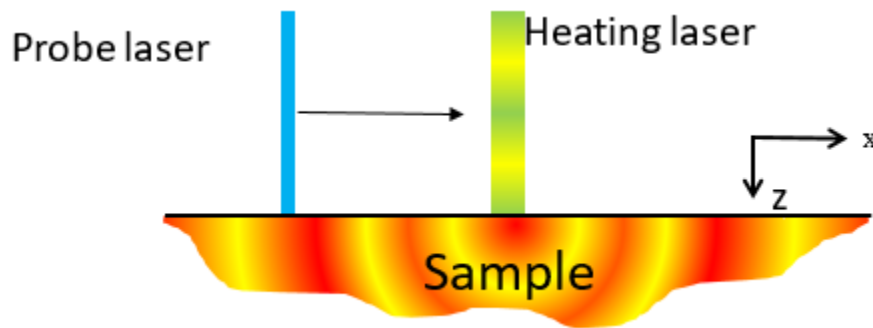
Figure 4.2: Schematic of the heating and probing lasers on a sample surface.

The spatial-scan photothermal reflectance technique operates on the basis that the

phase lag between the probe and heating lasers versus the laser separation distance is a

function of the material's thermal diffusivity. Namely:

$$\frac{d\varphi}{dx} = \sqrt{\frac{\pi f}{D}}$$

(4.13)

Where φ is the phase lag, x is the separation distance between the heating and

probe lasers, f is the frequency of the intensity of the heating laser, and D is the thermal

diffusivity. Therefore, by recording the phase lag corresponding to the distance between

the heating and detection spots, the thermal diffusivity can be extracted from $d\varphi/dx$ in

Equation 4.13, or the slope of the $\varphi - x$ curve in Figure 4.3. In typical photothermal

reflectance techniques, the phase diagram is generated by spatially scanning one of the

laser beams across the other. The slope of the phase diagram is also a function of the

frequency of the heat source. Figure 4.3 represents a combination of fitting curves

(theoretical plot of Equation 4.13), and experimental curves (markers). Each different

line represents a different heating laser frequency and thus each have a different slope.
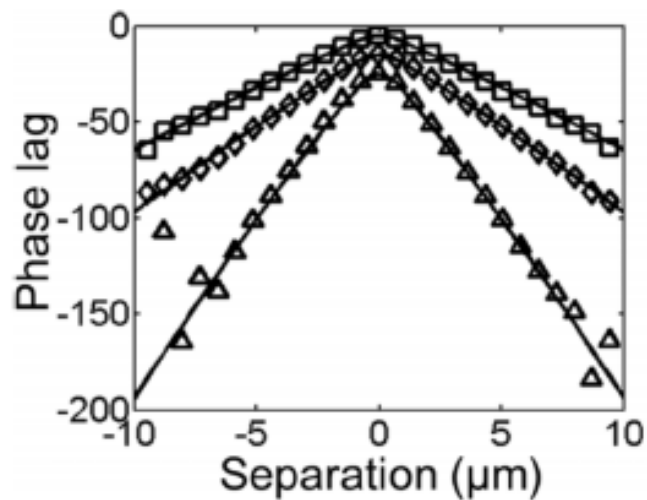
Figure 4.3: Experimental curves (markers) and fitting curves of the Phase Lag vs
Separation at Different Frequencies [38].

The same technique can be used for layered or coated samples. The model of this

scenario with its accompanying coordinate system can be seen in Figure 4.4. Equation

4.1 becomes a function of the thermal properties of both layers and the thickness of the

film substrate.
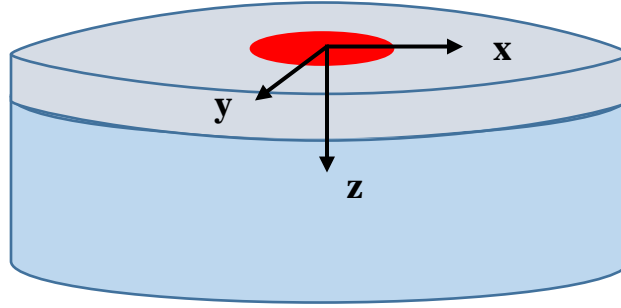
Figure 4.4: 3D Model and coordinate system.

By making the assumption that the film is a good thermal conductor, there is no temperature gradient in the depth direction in the film layer. The governing equations are as follows:

$$\rho_f c_f h \frac{\partial T_f}{\partial t} = k_f h \nabla_\perp^2 T_f + k_s \frac{\partial T_f}{\partial z} \qquad (4.14)$$

$$\frac{\partial T_s}{\partial t} = D_s \nabla^2 T_s \qquad (4.15)$$

where x represents the scan direction and z represents the depth direction.

By applying the method of separation of variables, $T = f(z) \cdot \exp(\phi x - i\omega t)$, the dispersion relation can be derived as

$$\phi = \sqrt{\frac{i\omega}{D_f} + \frac{\phi_0^2}{2} \left[1 - \sqrt{1 - \frac{4i\omega}{D_s \phi_0^2} \left(1 - \frac{D_s}{D_f} \right)} \right]} \qquad (4.16)$$

where $\phi_0 = -\frac{k_s}{hk_f}$

The "effective thermal diffusivity" of the layered sample can be defined to describe overall heat transport property as

$$Re(\phi) = \sqrt{\omega/2D_{eff}} \qquad (4.17)$$

By setting ω to high or low frequencies, it is determined that the real part of q becomes

$$Re(\phi) \approx Re\left(\sqrt{\frac{i\omega}{D_s}}\right) = \sqrt{\frac{\omega}{2D_s}} \tag{4.18}$$

in the low frequency range and

$$Re(\phi) \approx Re\left(\sqrt{\frac{i\omega}{D_f}}\right) = \sqrt{\frac{\omega}{2D_f}} \tag{4.19}$$

in the high frequency range.

In both the cases with a high and low frequency, the diffusivity can be determined in a simple manner. By adjusting the frequency of the heating laser to very high or very low frequencies, D_s or D_f can be measured separately. This is due to the fact that the thermal diffusion length is a function of the frequency, $L_{th} = \sqrt{\frac{D}{\pi f}}$. Lower frequencies will result in a larger diffusion length and thus a deeper penetration of the thermal wave. This allows for measurements of multilayered samples or samples that have coatings.

4.2   SSPRT for Kapitza Resistance Measurements

Up to this point, we have only considered models that are homogenous and are only capable of measuring the thermal diffusivity of a material. In order to derive the thermal resistance arising from an interface, a vertical thermal barrier must be introduced into the model, as seen in the following Figure 4.5.
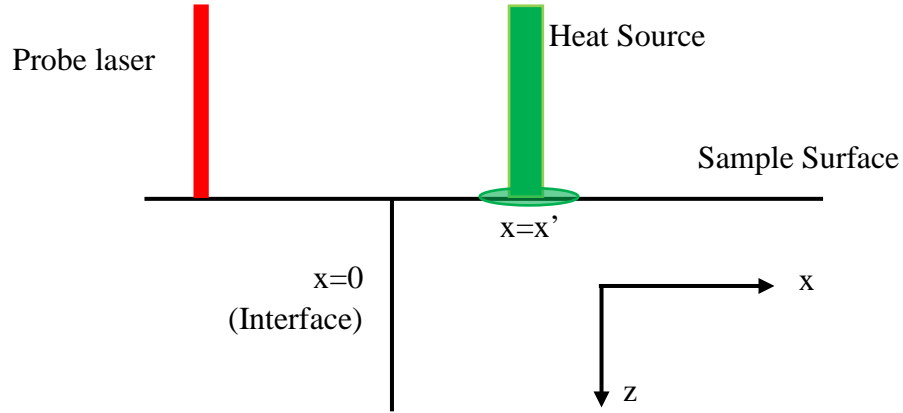
Figure 4.5: Geometry of the analytical model with the addition of a vertical boundary at $x = 0$ and heat source at $x = x'$.

The addition of this thermal barrier into the geometry will cause a perturbation of the temperature field. The solution found for the temperature distribution in the previous section is no longer accurate with the inclusion of the interface. The change of temperature at the sample's surface, assuming the heat source location is at $x = x'$ and the thermal resistance location is at $x = 0$, can be solved as [41,44]:

$$\Delta T(x) = R_k \left(\frac{P_0}{4\pi}\right) \int_0^\infty \exp\left(-\sigma|x| - \frac{p^2 R^2}{8}\right) (2$$
$$+ R_k k\sigma)^{-1} \left[\exp(-\sigma x') \, erfc\left(\frac{\sigma R}{2\sqrt{2}} - \frac{\sqrt{2}x'}{R}\right)\right.$$
$$\left. - \exp(\sigma x') \, erfc\left(\frac{\sigma R}{2\sqrt{2}} - \frac{\sqrt{2}x'}{R}\right)\right] dp \qquad (4.20)$$

where P_0 is the amplitude of the modulated heat flux, R_k is the thermal boundary resistance, p is the Hankel transformation variable, and σ is a function of p that is defined in the following relation:

$$\sigma = \sqrt{\frac{2\pi f i}{D} + p^2} \qquad (4.21)$$

Using Equation 4.20, the Kapitza resistance of the thermal interface can be

determined by its influence on the propagation of the thermal wave. The phase profile is

once again essential in determining thermal properties, including the thermal boundary

resistance. As the thermal wave spreads across the grain boundary, a phase shift is

generated by the Kapitza resistance. The phase profile is no longer continuous, but

experiences a phase drop at the location of the boundary. Figure 4.6 illustrates the same

theoretical phase graph as before as a result of Equation 4.13, but with a phase shift at

the origin. This apparent and sudden shift is due to the probe laser scanning over a grain

boundary at this location.
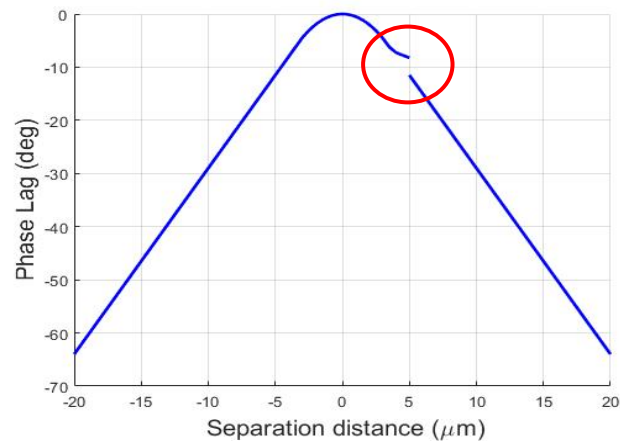
Figure 4.6: Theoretical phase profile with a phase shift due to a grain interface
at the $5\mu m$ mark.

Since the phase of the total temperature response is implicit in analytical

solutions, the thermal resistance extraction from the phase diagram curve requires a

multi-parameter fitting process that repeatedly solves Equations 4.11 and 4.20 at the same

time numerically for the best-fit solution. This fitting process is dependent on the

uniqueness of the best-fit solution and is affected by the experimental signal to noise

ratio, the sensitivity of the Kapitza resistance, and thermal transport properties of the

sample material. In order to implement Equation 4.20 and extract the thermal resistance,

other parameters need to be determined first. These include the thermal diffusivity,

conductivity, and the phase shift from the phase profile. The thermal diffusivity can be

determined by examining the slope of the phase graph at a location some distance away

from the grain interface and then comparing that slope to the inverse of the thermal

diffusion length. Once the diffusivity has been found, the conductivity can be calculated

by the relation $k = D\rho c_p$.

The phase shift can be extracted by way of examining the phase profile. The

background can be subtracted in order to easily determine the phase drop generated by

the thermal resistance and more clearly highlight the structure of the phase profile near

the interface. A theoretical example of this can be seen in the following Figure 4.7. The

phase profile is characterized by two distinguishing and related features, a slight raise

(η_1) in the phase profile followed by a phase drop denoted by (η_2). The second

characteristic, η_2, is of more significance and is essential in determining the Kapitza

resistance due to the grain interface.
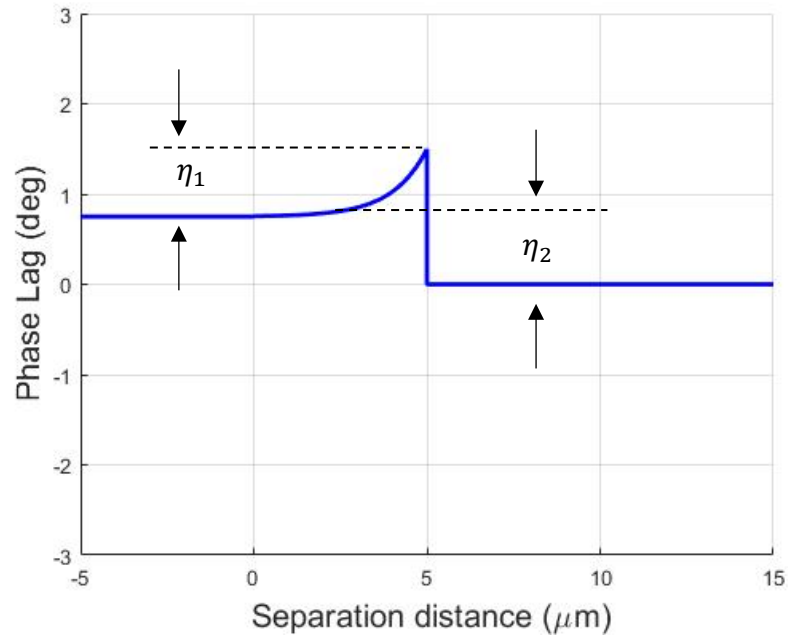
Figure 4.7: Theoretical model of a background free thermal wave phase profile across a grain boundary at the $5\mu m$ distance. Two distinguishing characteristics of the thermal wave phase profile near the interface are represented by η_1 and η_2.

After the phase shift has been determined, the thermal resistance of the grain boundary can be extracted using a multi-parameter fitting process in a straight forward manner. It is expected that for larger thermal resistances, there will be a larger phase shift generated in the phase profile.

Use of the photothermal optical reflectance technique to study interfacial thermal resistances has been done before. Hurley *et al.* [24] successfully used this method to measure the Kapitza resistance across a Si bicrystal interface. The geometry used for their model development is shown in the following Figure 4.8.
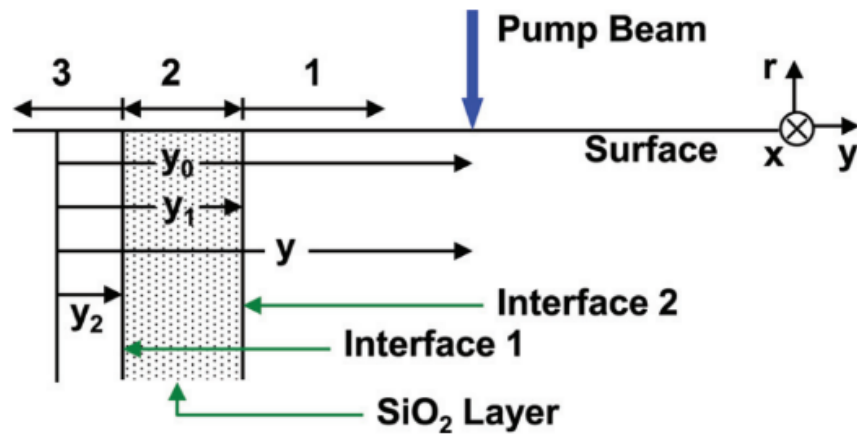
Figure 4.8: Geometry used for model development for a thin SiO_2 layer in between two interfaces [24].

The background free thermal wave phase profiles at one of the interfaces in this study can be seen in Figure 4.9. The pump laser was set at three different distances from the interface. The blue, solid line is experimental data while the dotted, red line is theoretical. The interface is represented by a vertical dotted line while the location of the heating laser is indicated by a blue arrow. In comparison to Figure 4.7, the rounded shape of the of the perturbation at the interface is due to the finite size of the probe beam. When the pump laser was placed on the interface, as seen in the top pane of Figure 4.9, the perturbation vanishes. If the phase shift were caused by deflection as a result of slight variations in topography near the boundary, the perturbation would not vanish. However, since it did vanish and because it moved in relation to the movement of the pump laser as seen in the middle and bottom pane in Figure 4.9, the phase shift of the phase profile is confirmed to be caused by the interface. This gives further validation that this technique

can in fact be used to determine the thermal resistance of interfaces, including naturally

occurring ones like grain boundaries.
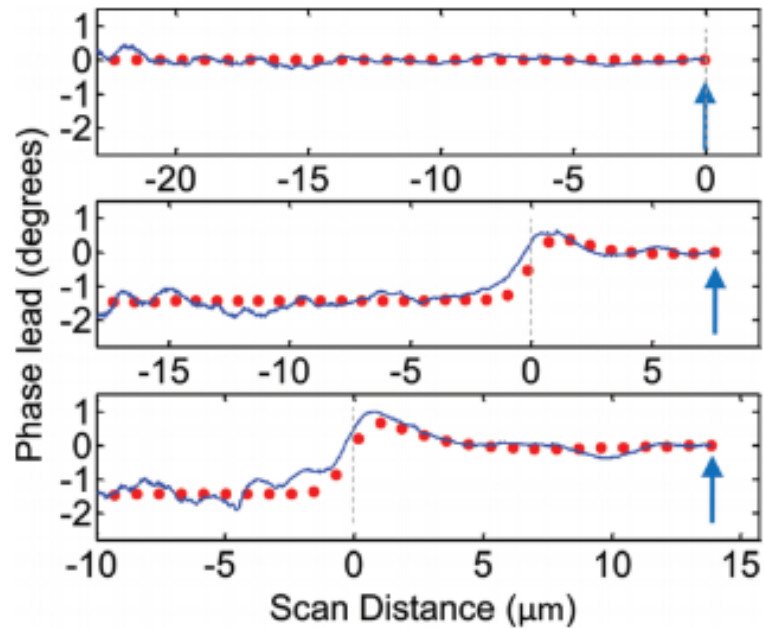
Figure 4.9: Phase profiles with subtracted backgrounds. The arrow and dashed line
represent the locations of the heating laser and interface, respectively [24].

Using the phase diagrams with the phase drop, the thermal diffusivity, and

thermal conductivity, Hurley *et al.* were able to measure a weighted average value for the

Kapitza resistance of the Si bicrystal interface to be $2.3 \cdot 10^{-9} m^2 K/W$.

Hua *et al.* [41] developed a similar method to measure the interface thermal

resistance using the photothermal technique in the frequency domain and obtained

comparable results, thus giving further confirmation that using the phase profile from a

photothermal reflectance technique is a viable method to determine the interfacial

thermal resistance.

This process of measuring the phase shift will be repeated at numerous crystalline interface sites on the sample surface of Cerium Oxide in order to statistically quantify the Kapitza resistance of its naturally occurring grain boundaries.

CHAPTER 5

EXPERIMENTAL PROCEDURE

The preparation details of the experiment are laid out in this chapter. The chapter is broken up into three parts which include the design and build of the experimental setup, the description of the sample, and the overall procedure.

5.1 Experimental Setup

The thermal phase profiles at the interface sites were generated using the following experimental setup, the design diagram of which is shown in Figure 5.1. Two continuous-wave lasers are used as both the heating laser (Laser Quantum Gem 532 with a mpc 6000 power supply) and the probe laser (CNI model MRL-III-671, DPSSl Driver). The power for the heating laser was set at 30 mW and the power for the probe laser was approximately 20 mW. However, the intensity of the lasers is diminished after they pass through multiple optics such that the remaining power that reaches the surface of the sample is only a percentage of the initial exit power. The frequency of the heating laser for all measurements was set at 50 kHz, which is controlled by a function generator (Agilent Technologies 3320A). An acousto-optic modulator (AOM, Gooch and Housego R35085-3 with the driver model R31085-6AS) was used for the heating laser to control the amplitude modulation. An AOM uses the acoustic-optic effect to diffract and shift the frequency of light using sound waves. These modulators are typically used in lasers for Q-switching, which is a technique by which the laser can generate an oscillating out-beam. This is necessary for this experiment in order to produce a harmonic thermal wave and generate resulting phase profiles. In order to scan the probe laser relative to the

pump laser, the probe laser is passed through a pair of confocal lens. The first lens is mounted on a motorized stage (Newport Motion Controller Model ESP301) in order to allow movement of the probe laser beam on the x-y plane. The second lens converts the x-y motion of the beam into an angle change as it enters a 50X objective lens (Nikon L Plan SLWD 50X/0.45). The heating laser is focused on the center of the objective lens using a dichroic mirror. The positions of the probe laser and the heating laser on the sample surface are observed and checked from a CCD camera (ThorLabs DCU223M). After passing a bandpass filter to block the pump laser, the reflected probe beam is collected by a photodetector (New Focus nanosecond photodetector 1621). The signal from the probe beam is amplified and analyzed by a lock-in amplifier (Stanford Research System SR844). The lock-in amplifier is a type of amplifier that can extract a signal from an extremely noisy environment. They are used to detect and measure very small AC signals and accurate measurements can be made even when the small signal is obstructed by a noisy background. Nosie signals that are at frequencies other than the reference frequency are rejected and do not alter the measurement. Lock-in amplifiers are commonly used to measure phase shifts, which is the intended application of this experiment. All of the resulting data is analyzed using MATLAB, including generating phase profiles and amplitude graphs. Experimental parameters such as scan distance and time constants are set in MATLAB
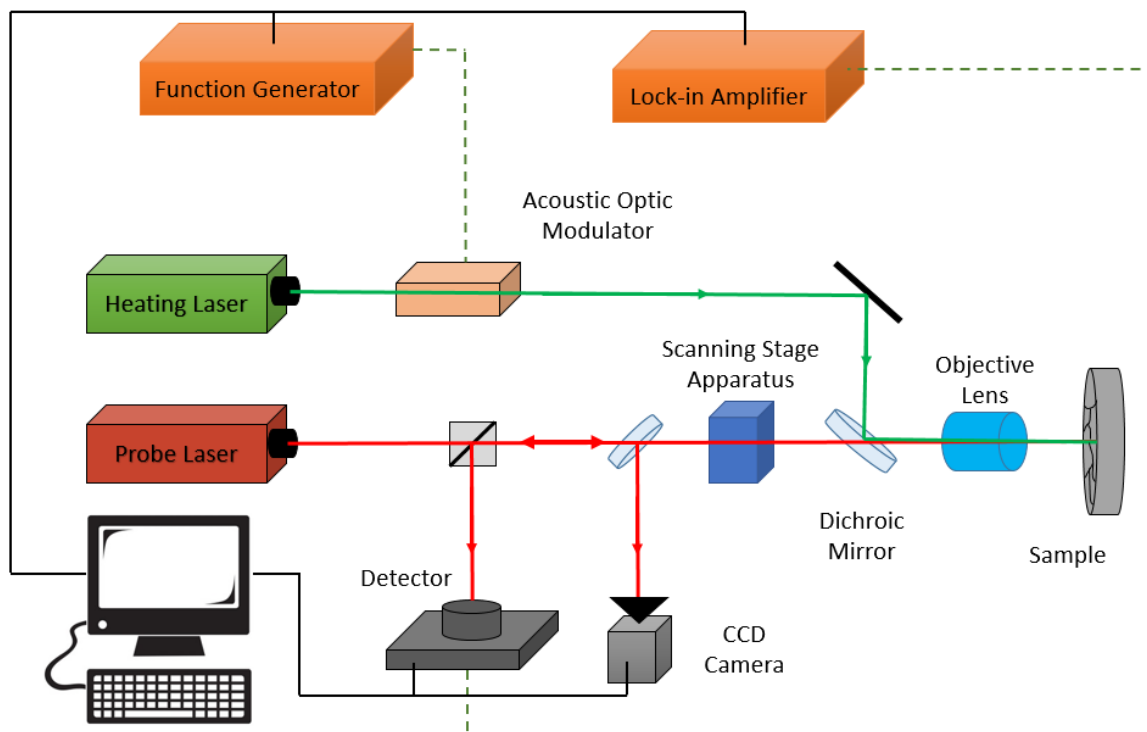
Figure 5.1: Diagram of the experimental setup.
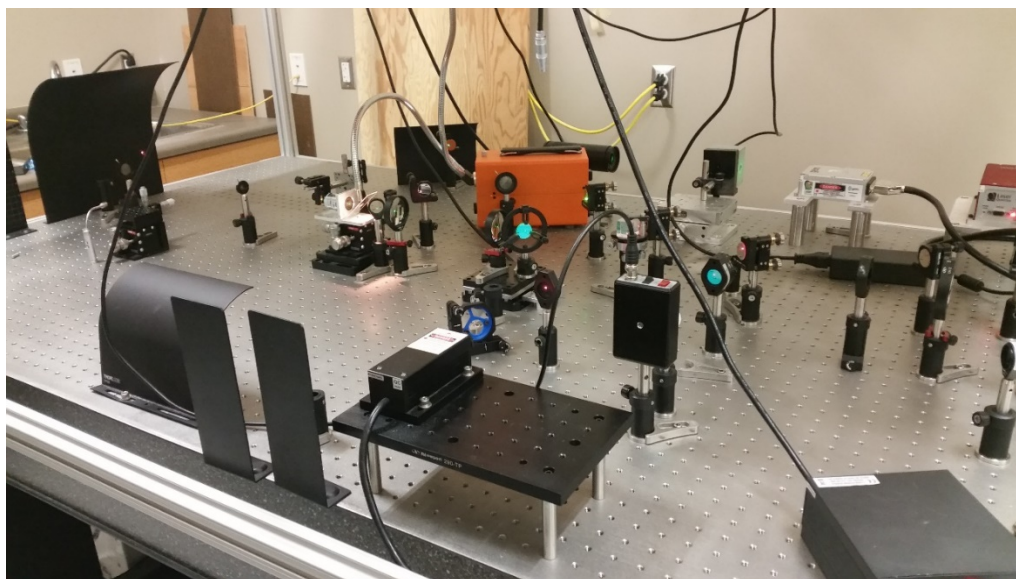
Figure 5.2: Physical experimental setup.
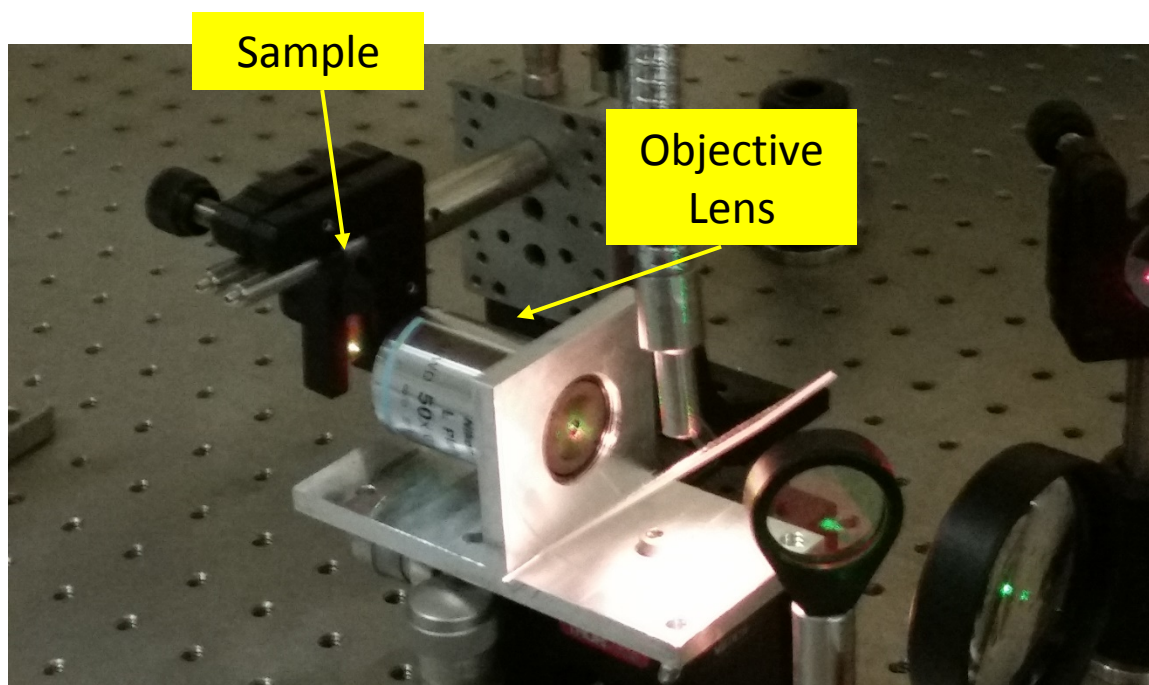
Figure 5.3: Experimental setup showing sample and objective lens.
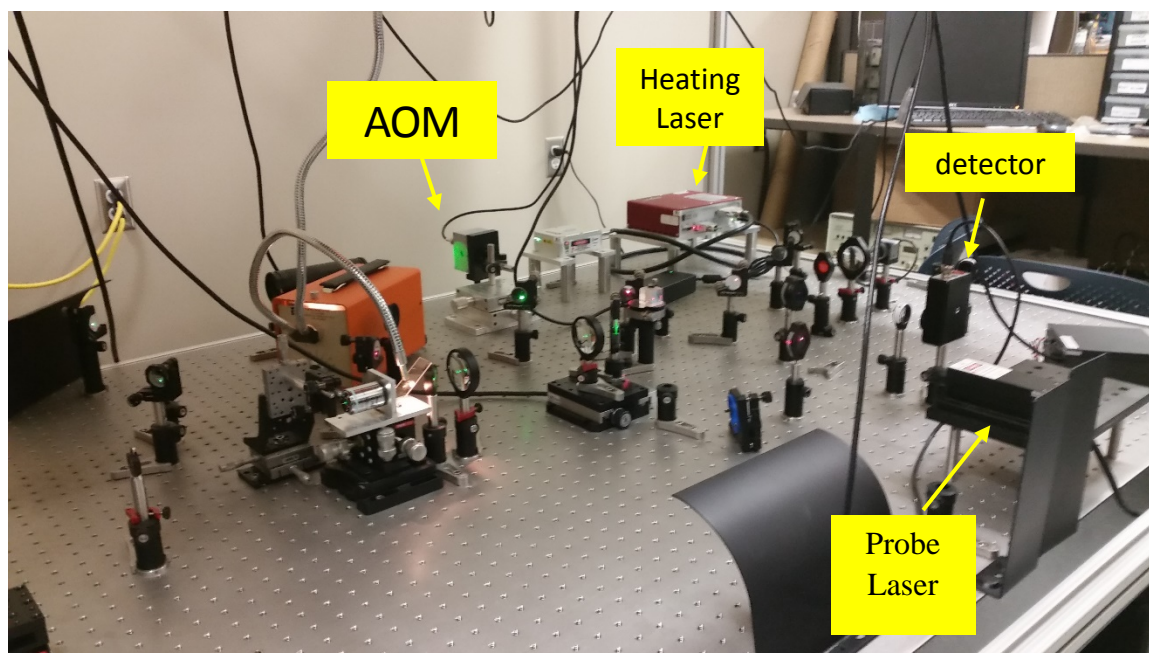
Figure 5.4: : Experimental setup showing lasers, detector, and AOM.
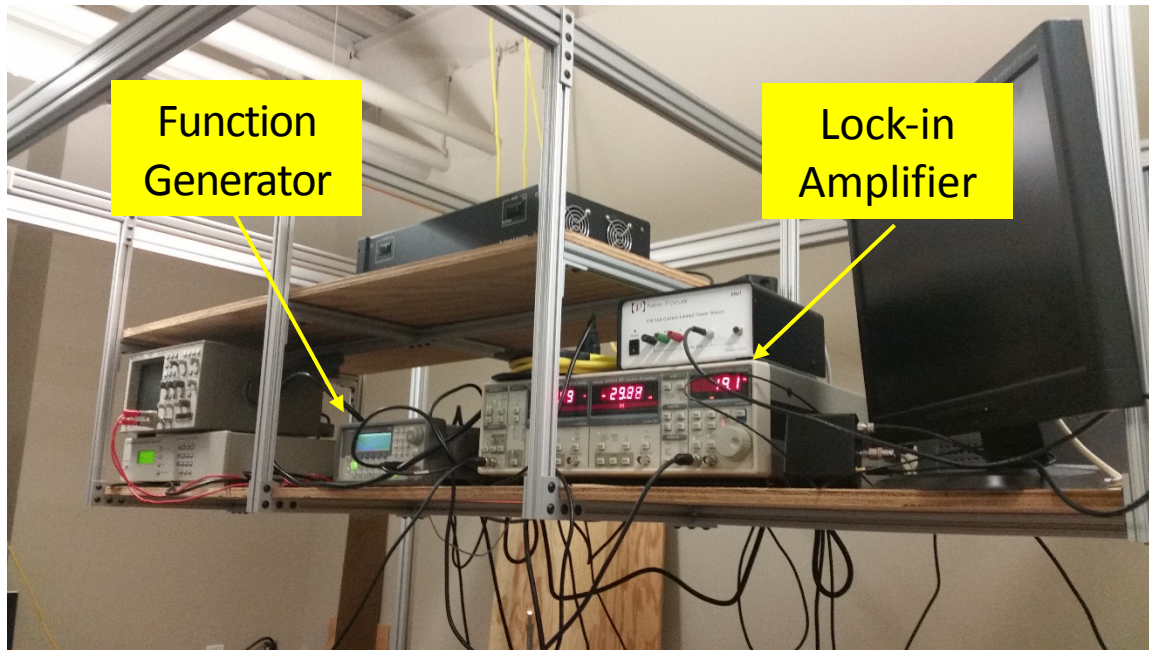
Figure 5.5: Function generator and lock-in amplifier.

5.2 Sample Description

The following section details and describes the specimen measured in this experiment. A photo of the sample can be seen in Figure 5.6 below (coin added for size comparison). The sample measures approximately 1 *cm* in diameter and has a thickness of 1 *mm.*

The sample specimen of CeO_2 was provided by the University of Florida. The pellet was fabricated using an isostatic pressing and sintering process. This involves subjecting the material (initially a powder like what is shown in Figure 5.7) to an elevated temperature and an isostatic gas pressure in a high pressure containment vessel.

Figure 5.6: Sample pellet (penny included for size comparison).

Figure 5.7: CeO$_2$ in powder form before sintering [45].

This process of compacting and forming the material by means of high heat and high pressure converts the powder form of CeO_2 into a solid sample. The average grain size of the sample is approximately 50 μm and the theoretical density is 96%. The sintering process was carried out at 1600°C and was followed by a high temperature annealing at 1800°C in air for 4 hours. The CeO_2 sample was subjected to a Kr implantation at 200 and 600°C with the damage doses ranging from 0.3 to 150 displacements per atom. After the fabrication process, the sample surface was coated with a thin layer (50 nm) of titanium in order to improve the absorption and thermoreflectance effect. The grain structure of the sample in its solid form can be seen below in Figure 5.8.
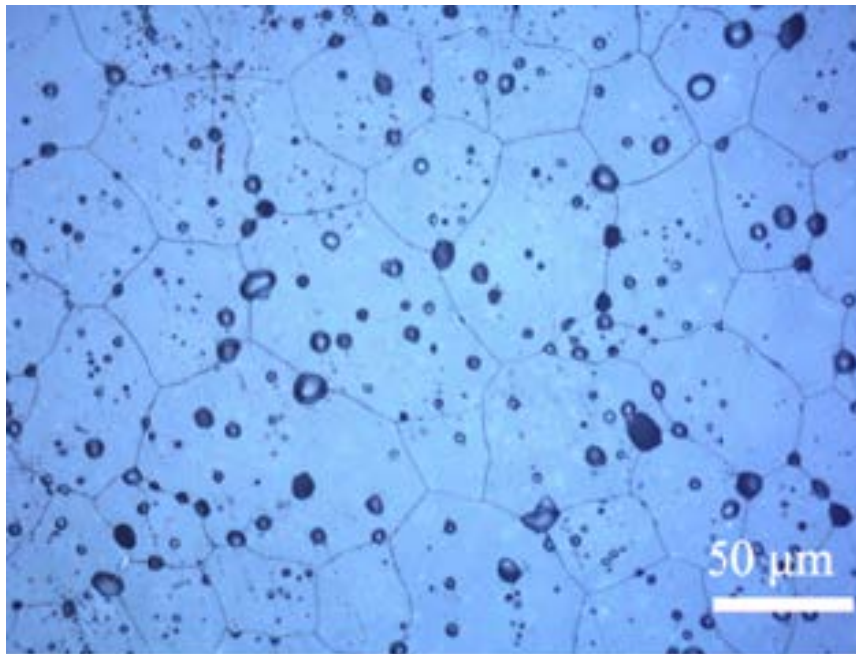
Figure 5.8: Microstructure of the solid CeO_2 pellet. The air voids
are a result of Kr implantation.

A summary of the size and other parameters of the sample of CeO_2 are tabulated in the following Table 5.1.

Table 5.1: Summary of the specifications of the sample specimen.

Parameter	Value
Sample Size	Diameter $= 1$ cm, thickness $= 1$ mm
Porosity	96%
Average grain size	50 μm
Ti coating	50 nm

5.3 Experimental Procedure

The following section outlines the steps taken to characterize the thermal resistance across the grain boundaries of the sample of CeO_2.

1) Align the Modulated Optical Reflectance (MOR) system, align the sample, and find a target interface.

The MOR system is very sensitive, and therefore in order to obtain the best and most accurate results, both the heating laser and probe laser must be properly aligned. This can be accomplished with the use of adjustable mirrors and continuously variable iris diaphragms. After the lasers have been aligned, the Cerium Oxide pellet is then inserted in the sample holder and aligned such that it is perpendicular to the laser profile. The sample is also adjusted so that it is at the optimal distance to the objective lens to achieve the highest resolution and best results. Using the CCD camera, suitable grain boundaries, such as the one immediately to the right of the green heating laser in Figure 5.9, are identified. Interfaces appropriate for measuring are relatively long, straight, and perpendicular to the probe laser scan direction. A suitable section of the interface is

identified for measuring. Interfaces that are relatively long, straight, and clear of air

voids are desirable.
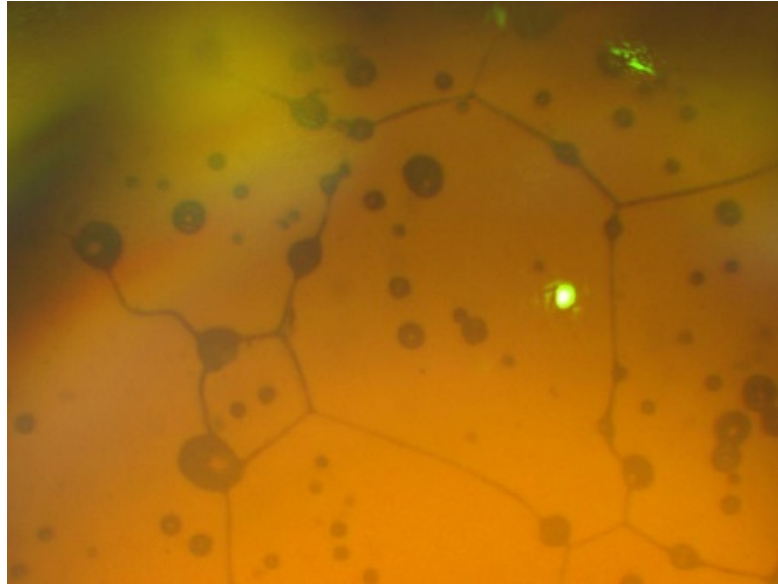
Figure 5.9: Typical target grain boundary used in the experiment. It is directly to
the right of the green pump laser.

2) Obtain phase profiles.

After the MOR system and the sample have been properly aligned and a target

interface identified, the thermal wave phase profile can be generated. The heating laser is

set 4 μm to the left of the grain boundary. The initial position of the probe laser is set on

top of the heating laser so that the peak of the thermal wave phase profile will be at the

origin. The probe laser is also aligned relative to the heating laser on the sample surface

such as to obtain the highest voltage signal of the lock-in amplifier. The probe laser can

then be scanned across the heating laser and across the grain boundary to generate the

phase lag versus laser separation plot with the resulting phase shift due to the interfacial

thermal resistance. Because of the high signal to noise ratio and in order to eliminate experimental error, the process of measuring the phase profile is repeated multiple times at the same location.

      3) Determine thermal diffusivity and phase drop.

After the phase profiles for a target location have been measured, the plots with clean data can be averaged into a single phase profile from which the thermal diffusivity and the resulting phase drop generated by the Kapitza resistance can be obtained. The thermal diffusivity is calculated by setting the slope of the phase profile equal to the thermal diffusion length, as in Equation 4.13. The background can then be subtracted from the phase profile and the phase drop can be extracted in a straightforward manner by observing the resulting graph.

      4) Extract Kapitza resistance.

After the thermal diffusivity and phase drop have both been calculated, a multi-parameter fitting process that repeatedly solves Equations 4.11 and 4.20 can be used to quantify the resistance across the targeted grain boundary. The solving of the two aforementioned equations is done numerically using MATLAB. The thermal conductivity is also necessary in order to determine the Kapitza resistance.

      5) Repeat experimental process for multiple boundaries.

Steps 1-4 are repeated at different interface sites. In this study, approximately 80 target boundaries were selected and an averaged phase profile was generated for each as well as the resulting Kapitza resistance. The purpose was to perform a statistical analysis in order to ensure confidence in the measured results and minimize experimental error.

The average Kapitza resistance was then compared to values found in literature for further validation of the results of the experiment.

CHAPTER 6

RESULTS AND DISCUSSIONS

In this chapter, the experimental results are given. All steps generally follow the outline given in Section 5.3. The phase profile at the location of a target grain boundary was acquired using the MOR system, and using the resulting slope and phase drop from those phase profiles, the Kapitza resistance was determined using a multi-parameter fitting process in MATLAB.

6.1   Thermal Phase Profiles

After identifying a target boundary using the CCD camera, the experimental setup was used to carry out measurements at the relatively high frequency of 50 kHz. This frequency was chosen to ensure that the thermal wave would pass through the titanium coating and that only the properties of the CeO_2 sample would affect the phase profile. A simple calculation using the thermal diffusion length relation, $L_{th} = \sqrt{\frac{D}{\pi f}}$, confirms that this is an appropriate frequency at which to take the measurements. Using the properties of titanium and the frequency of 50 kHz, the thermal diffusion length is ~8 μm. The coating of titanium is only 50 nm. Thus, the thermal wave will easily penetrate past the coating and into the CeO_2.

The scan distance of the probe laser across the pump laser was set at 20 μm. The heating laser is fixed at a position 4 μm to the left of the target interface, as can be seen in Figure 6.1. A 50X long working distance objective lens was used to focus the two lasers and gain higher resolution. Both the heating laser and the probe laser beams have a

diameter of several millimeters before being focused and only $1 - 1.5\ \mu m$ after being

focused on the sample surface.
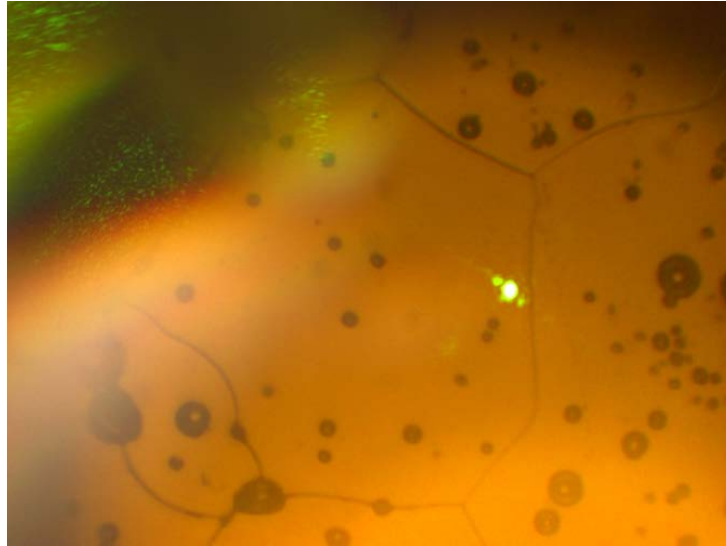
Figure 6.1: Target grain boundary with heating laser set 4 µm to the left of the interface.

Multiple measurements are taken at the target location in order to decrease

experimental errors. Good data with minimal noise is averaged into a single plot. Figure

6.2 shows the six separate measurements that were taken at the target site from Figure

6.1. Figure 6.3 is the averaged plot of the six measurements. The dashed line at the $4\ \mu m$

mark represents the grain boundary. The thermal diffusivity can be found from the slope

of this phase profile so long as it is measured some distance away from the grain

boundary.
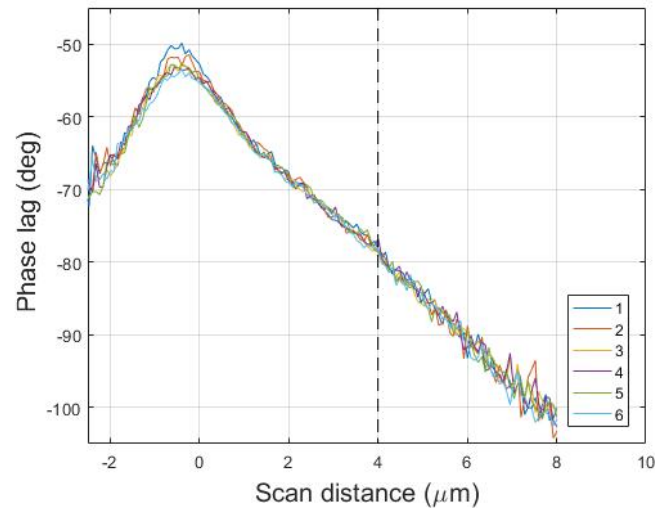
Figure 6.2: Phase profiles generated at the target boundary from Figure 6.1. The location of the grain interface is represented by the dashed line.
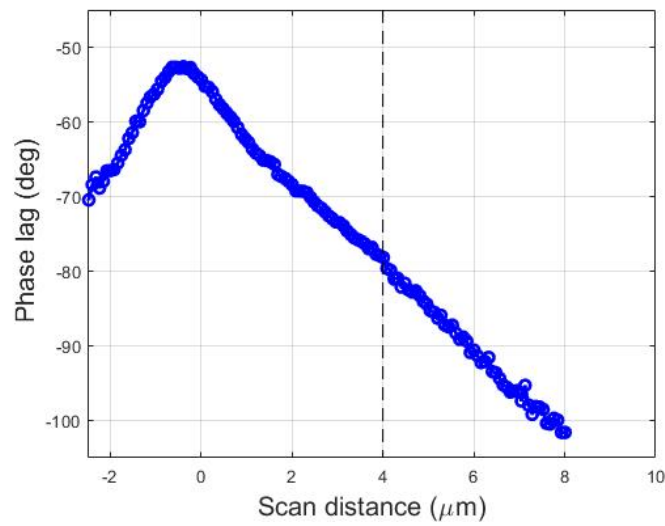
Figure 6.3: Averaged phase profile.

The following Figure 6.4 represents the average phase profile with the subtracted background at the location of the grain boundary from Figure 6.1. Two different trend

lines have been added before and after the 4 μm mark to show the movement of the profile. The experimental profile agrees well with the theoretical plot from Figure 4.7. There exists a small raise in the profile followed by the phase drop, the latter of which is the important parameter for the experiment.
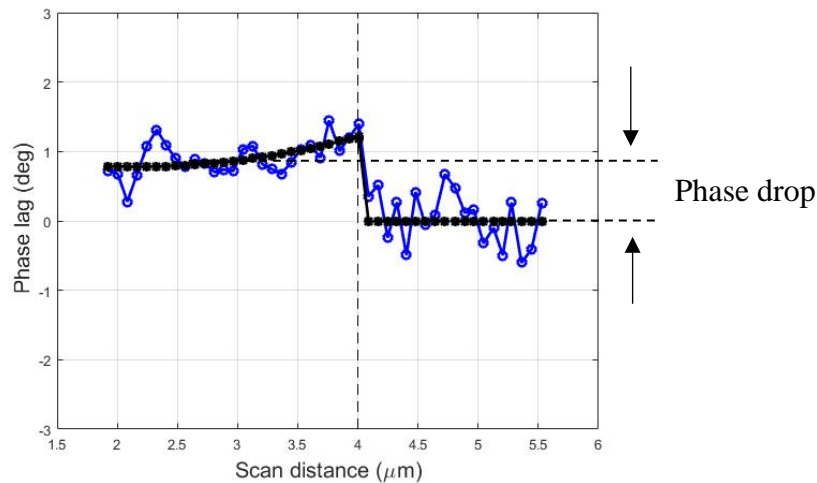
Figure 6.4: Phase profile with subtracted background, trend lines, and phase drop. A second order polynomial trend line was used as a trend line for the first segment.

The last parameter to be found is the thermal conductivity. This value is typically determined by using Equation 1.3 ($D = \dfrac{k}{\rho c_p}$). For this study, it was determined using the direct relationship of thermal conductivity to thermal diffusivity found in literature [21,20]. Assuming constant values of specific heat and density between the sample in this experiment and those in the aforementioned studies, at room temperature the relationship between thermal conductivity and diffusivity of CeO_2 is $k \cong 3 \cdot D$. Using this relation, the fitting process is then used to extract the thermal resistance.

6.2 Measured Results

The following Table 6.1 shows the average measured results for this study.

Table 6.1: Averaged measured values.

Parameter	Average Value
$D \ (m^2/s)$	$12.6 \cdot 10^{-6}$
Phase lag (deg)	1.15
$R_k \ (m^2 K/W)$	$9.88 \cdot 10^{-9}$

Of the approximately 81 different boundary sites measured, 23 sets of data were unusable because of extremely noisy data, no apparent phase drops, or because of relatively large discrepancies in measured values of thermal diffusivity between adjacent grains. The multi-parameter fitting process requires that the two grains that share a boundary must have relatively similar values of thermal diffusivity. If the differences in diffusivity are too great, the thermal boundary resistance cannot be calculated. This leaves approximately 58 sets where the two grains have similar thermal properties and there is an obvious phase drop that can be seen and calculated from the phase profile. Excluding a few extreme outliers, the measured average Kapitza resistance across the grain boundaries of the CeO_2 sample is $9.88 \cdot 10^{-9} \ m^2 K/W$.

The following histogram from Figure 6.5 displays the measured results of the 53 different grain boundary sites used to determine the average Kapitza Resistance. A

discussion of the results follows in the next section.
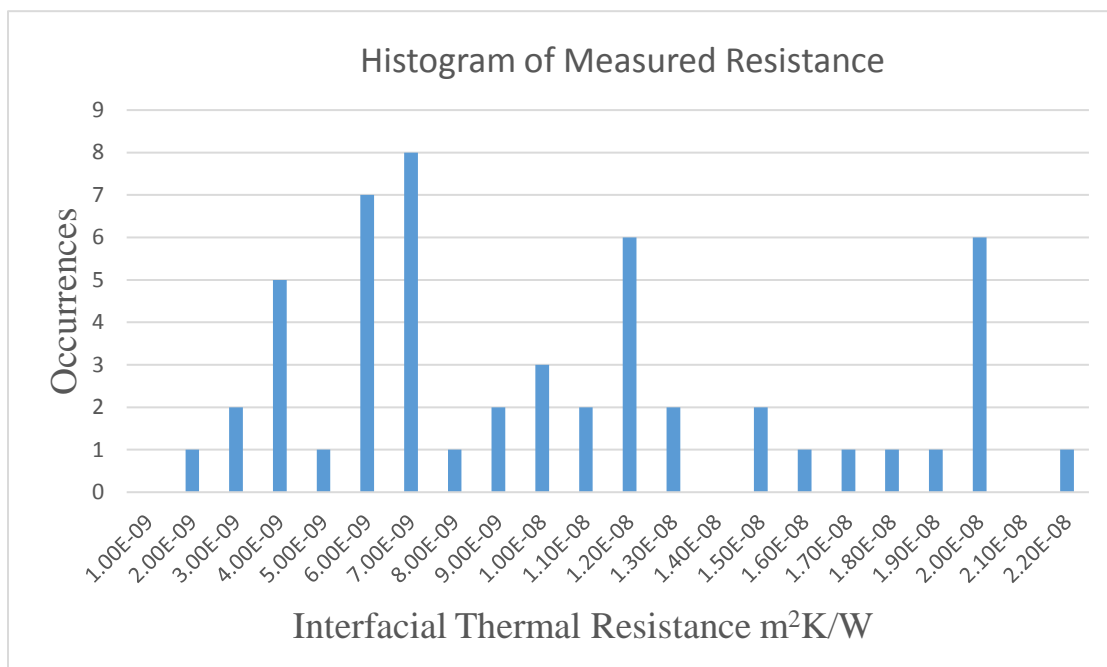
Figure 6.5: Number of occurrences of the values of the Kapitza resistance measured at 53 different grain interface locations.

6.3   Discussion on Results and Experimental Errors

This section presents a detailed discussion on the results of the experiment, as well as a comparison to other values found in literature and a discussion on the experimental error.

6.3.1   Discussion

While there has been relatively little work done previously on determining the thermal resistance across grain boundaries of CeO_2, there are a few sources that can be checked in order to help determine the validity of the results of this thesis experiment. Previously discussed in Chapter 2, Khafizov *et al.* [21], using the effective medium

model, measured the weighted average of the room-temperature Kapitza conductance of CeO$_2$ to be $0.036\ GW/m^2K$. The inverse of this value is the Kapitza resistance. This value for the measured Kapitza resistance is then $2.77 \cdot 10^{-8} m^2K/W$, which is relatively close to the average value of $9.88 \cdot 10^{-9} m^2K/W$ measured using the SSPRT in this experiment. Khafizov *et al.* also used non-equilibrium MD simulations to determine the Kapitza conductance of different grain boundary types. The following Table 6.2 contains their results, and shows the inverse of the values of the Kapitza conductance presented in Table 2.1 to display the Kapitza resistance for direct comparison to the results of this thesis study.

Table 6.2: Kapitza Resistance at different grain orientations using MD [21]**.**

Grain-boundary type	Kapitza resistance (m^2K/W)
Σ3	$0.435 \cdot 10^{-9}$
Σ11	$0.37 \cdot 10^{-9}$
Σ13	$0.303 \cdot 10^{-9}$
Σ3 ($UO_2\ at\ 800K$)	$0.625 \cdot 10^{-9}$

The average Kapitza resistance measured using the SSPRT in this thesis study falls in the range of the measured value and MD simulated values found in the Khafizov *et al.* study, but is relatively closer to the measured value and is an order of magnitude greater than the MD values.

Another study that was reviewed in Chapter 2 and one that can be used for direct comparison to this experiment is that of Watanabe *et al.* [26]. In that study, the thermal transport properties of UO$_2$ by MD simulations are investigated. Using two different

models, they obtained room-temperature values for the Kapitza conductance to be

0.15 GW/m^2K and 0.3 GW/m^2K, the inverse of which and the resulting Kapitza

resistances are 6.66 $\cdot 10^{-9} m^2 K/W$ and 3.33 $\cdot 10^{-9} m^2 K/W$, respectively. The former

resistance is closer in value to the measured value found in this thesis study, and although

it is a different material, it helps validate the results found using the SSPRT since UO_2

and CeO_2 have many similar thermophysical properties.

    While the average value matches relatively well with certain literature studies,

there was still a wide range of resistances that were measured, as can be seen from the

histogram in Figure 6.5. There are multiple reasons as to why there could be

discrepancies in the measured values.

    One of the anomalies noted in this experiment was not only the wide range of

thermal resistances measured, but also a wide range of values of thermal diffusivity,

which in turn affect the calculated values of Kapitza resistance. Measured values for the

thermal diffusivity were in the range of $6.5 \cdot 10^{-6} \ m^2/s \ - \ 31 \cdot 10^{-6} \ m^2/s$. These

values of thermal diffusivity are then used to calculate the Kapitza resistance and

therefore a wide range of thermal diffusivities can lead to a wide range of measured

thermal resistances. The wide range of diffusivities, especially the higher values, was

unexpected and can most likely be attributed to the sensitivity of the MOR system and

experimental error. The average measured value of the thermal diffusivity was $12.6 \cdot 10^{-6} \ m^2/s$, which was higher than anticipated.

    An extremely likely explanation as to why there is a wide range of measured

resistances can be related to the different types of grain boundaries and different

boundary angles in CeO_2. Not all grain interfaces are the same and do not display the same grain misorientation relationship. Different grain boundaries most likely scatter phonons and interfere with heat energy transfer to differing degrees. Large-angle grain boundaries, characterized by more dislocations and regions of larger disorder, may have a larger effect on heat flow when compared to low-angle grain boundaries. Also, the grain boundaries could very well be slanted in the *y-z* plane and affect the thermal wave differently. Other dislocations and oxygen vacancies can contribute to the disruption of the heat flow too. The sample pellet very well may be non-stoichiometric and thus a small percentage of atoms may be missing from the microstructure creating voids or vacancies. The opposite may be true too where there are too many atoms packed into an otherwise flawless lattice structure. Because of the different types of grain boundaries, a range of measured thermal boundary resistances should be expected.

Since only the surface of the sample can be seen using the CCD camera, it is impossible to know for sure what is underneath and what exactly the thermal wave is interacting with. There could be other grain boundaries, large air voids as a result of the Kr implantation, or other impurities close to the surface interfering with the thermal propagating wave. While the frequency was purposely set at a value of 50 kHz in order to limit the thermal penetration depth and thus avoid this potential problem, it is still a feasible explanation as to why there exists a discrepancy in the measured values.

6.3.2 Uncertainty and Experimental Errors

There exist a few sources of uncertainty regarding this experiment and are explored in this section.

One source of uncertainty stems from the process of subtracting the background from the phase profile in order to determine the thermal diffusivity and phase drop. Decreasing or increasing the physical range over which an average phase difference was calculated changed the results significantly in some cases. Including or excluding an extra data point could alter both the phase drop and diffusivity. The following Figure 6.6 seeks to illustrate the effect that this has on the overall results. Each line represents a different thermal diffusivity. At small phase drops, there is a minor difference in measured Kapitza resistances between differing diffusivities. However, as the phase drop increases, so does the difference between lines. This goes to show that the multi-parameter fitting process is more sensitive to different thermal diffusivities at higher phase drops.
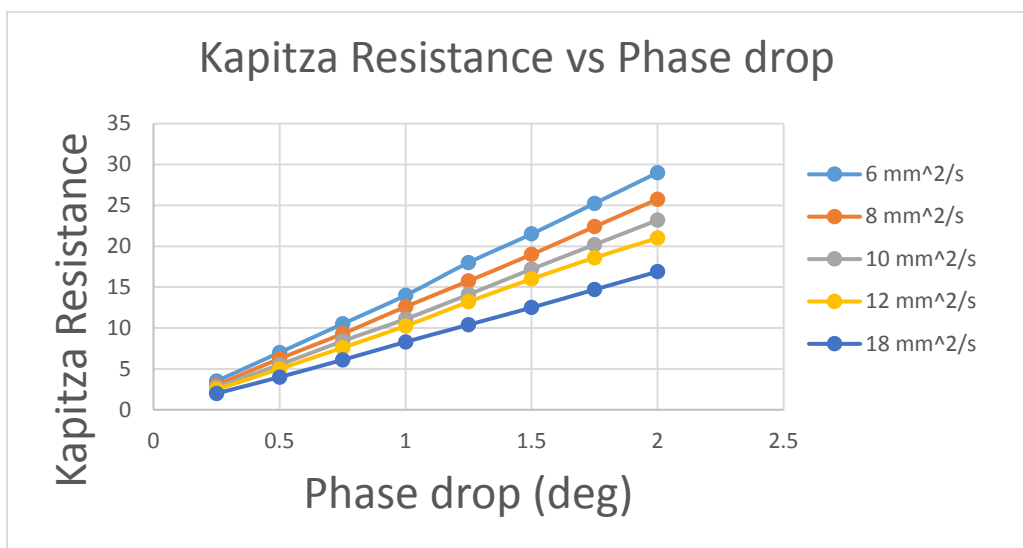

Figure 6.6: Kapitza resistance vs phase drop for different thermal diffusivities.

One of the anomalies of this thesis experiment was measuring relatively high values of thermal diffusivity compared to those found in literature. The average thermal diffusivity measured in this study was $12.6 \cdot 10^{-6} \ m^2/s$, which is nearly double that found in literature [21]. At small phase drops less than 1 degree, this difference results in a relatively minor change to the calculated thermal resistance. However, this change becomes more pronounced at higher phase drops. Since the average thermal diffusivity in this experiment is anomalously large compared to other studies, it is possible that the actual average Kapitza resistance is higher than the measured value found in this thesis study. However, this should have no effect on the measured phase drops, and therefore measured Kapitza resistances from this experiment should still be relatively close to the true value. Also, if the true values of thermal diffusivity in the grains in this experiment are indeed smaller than the measured values, this would just result in a slight shift to the right of the bars in histogram from Figure 6.5.

A few other anomalies had to be considered when conducting this experiment. The multi-parameter fitting process requires that the two adjacent grains that share a boundary must have relatively the same thermal diffusivity. If they do not, the resistance cannot be extracted. Figure 6.7 is a phase profile with the background subtracted. Because of differing diffusivities between grains, there exists a sharp slope change at the grain interface. No phase drop can be detected and the thermal resistance cannot be determined from this particular interface site.
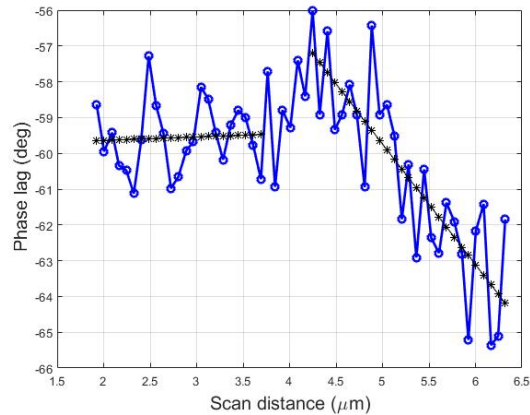
Figure 6.7: Phase profile with different thermal diffusivities between adjacent grains.

While the average phase drop at interfacial locations was 1.15 degrees, there were a few extreme cases where the phase shift was much larger. The measured phase drop at one particular site was 5.46 degrees. This results in a measured resistance of $6.95 \cdot 10^{-8} m^2 K/W$ and was the most extreme case. Probable causes of this is burning of the sample due to repeated scans of the laser, air bubble voids from the Kr implantation below the sample surface or integrated into the boundary itself, or surface topography defects. There were only a handful of these extreme cases and they were not used to calculate the average thermal boundary resistance.

CHAPTER 7

CONCLUSIONS AND FUTURE WORK

This final chapter presents the conclusions and discusses potential future work.

7.1   Conclusions

The purpose of this thesis experiment was to determine the Kapitza resistance across grain boundaries of CeO$_2$ using the SSPRT. The average measured thermal boundary resistance is $9.88 \cdot 10^{-9}\ m^2 K/W$. While there is a level of uncertainty regarding this measurement, it does agree well with values found in literature from experiments and MD simulations. Because the measured thermal diffusivity was anomalously large, it is proposed that the actual value of the Kapitza resistance may be larger than what was measured, possibly even an order of magnitude greater.

There was a wide range of resistances measured at interface sites on the sample. This is to be expected though, as not all grain boundaries are the same and some will impede heat flow more than others based on grain boundary width and boundary angle. Those boundaries with higher angles will present regions with greater atomic mismatch and thus scatter phonons to a higher degree than those of lower angles

The SSPRT was the chosen method to measure the resistances and proved suitable to measuring the phase profiles at high spatial resolutions. Noticeable phase drops were recorded and used to extract the thermal resistances.

7.2   Future Work

There exists potential future work for this type of study. As mentioned previously, there is an expected correlation between grain boundary resistance and types of grain boundaries. The exact relationship of how the Kapitza resistance is a function of grain boundary angle is one that can be explored in more detail. This can be done by first determining the orientation of the grains by electron backscatter diffraction (EBSD). EBSD is a technique which can obtain accurate crystallographic information from materials, such as identifying grain orientations and grain boundaries.

Preliminary work was done in order to test the theory that there is a relationship between grain angles and thermal boundary resistance. Five grain boundaries were measured using the SSPRT to determine their thermal resistance. The exact locations of the grain interfaces were carefully recorded so that they could be relocated using a scanning electron microscope (SEM). After the thermal boundary resistance was measured, the titanium coating was removed from the sample surface using a chemical solution. A magnified image of the sample surface at one of the grain boundaries was then taken using the SEM, and can be seen with its accompanying grain orientation map and Inverse Pole Figure (IPF) Z in Figures 7.1 through 7.3.
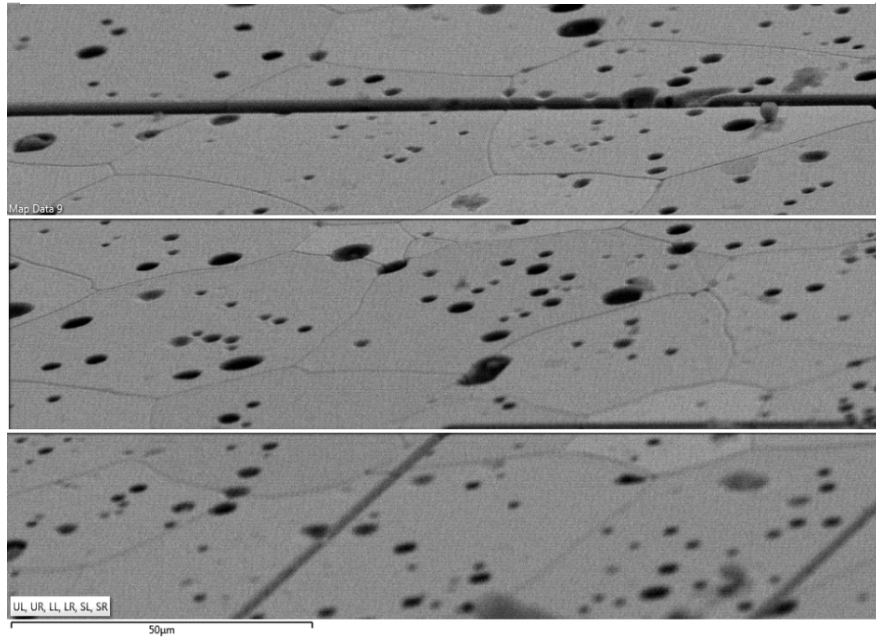
Figure 7.1: SEM image of the sample surface.
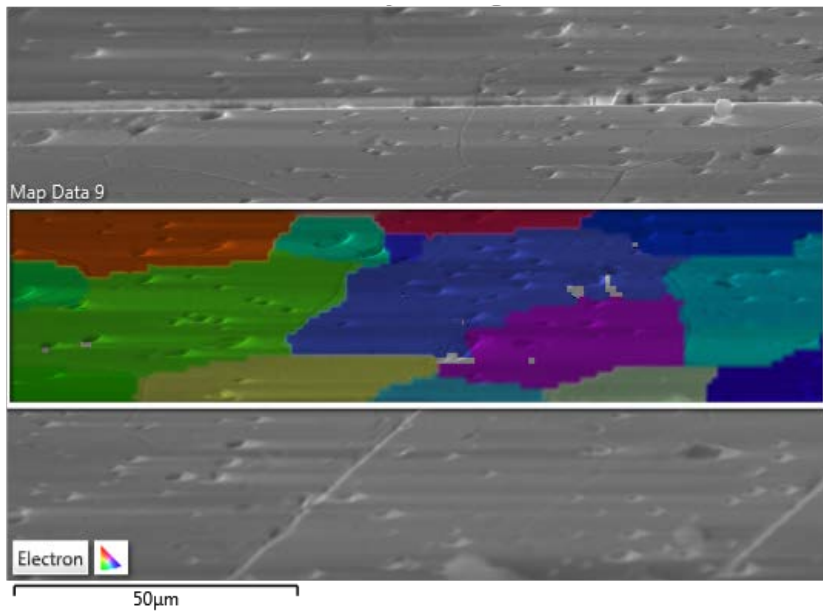
Figure 7.2: EBSD layered image.
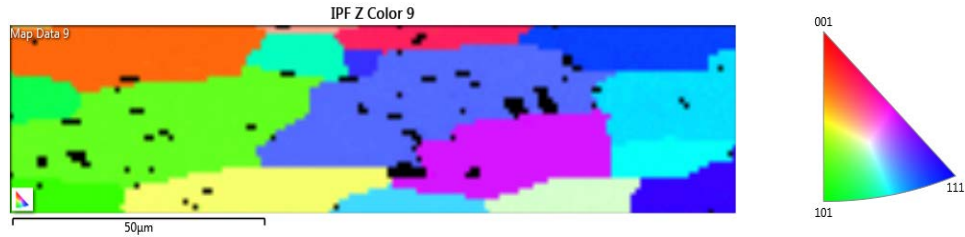
Figure 7.3: IPF Z showing different grain orientations.

After identifying the grains and their respective orientations, the angles of the target grain boundaries were determined. The following Figure 7.4 shows the measured Kapitza resistances versus the respective measured boundary angles of the five target interfaces. There exists a general upward trend that would suggest that higher grain boundary angles lead to larger thermal boundary resistances. This is supported by a few other studies as well [46,47].

Figure 7.4: Kapitza resistance vs grain boundary angle.

Because of the time consuming nature of this process, only five interfaces could be measured. Using the EBSD can take a long time to generate the orientation map. The process increases in complexity due to the difficulty of relocating grains when transitioning between the EBSD microscope and the MOR system. Also, the titanium coating has to be removed using a chemical solution that will not affect the sample. This means that all thermal measurements must be done before the grain angles can be determined. However, the process is doable as proven above a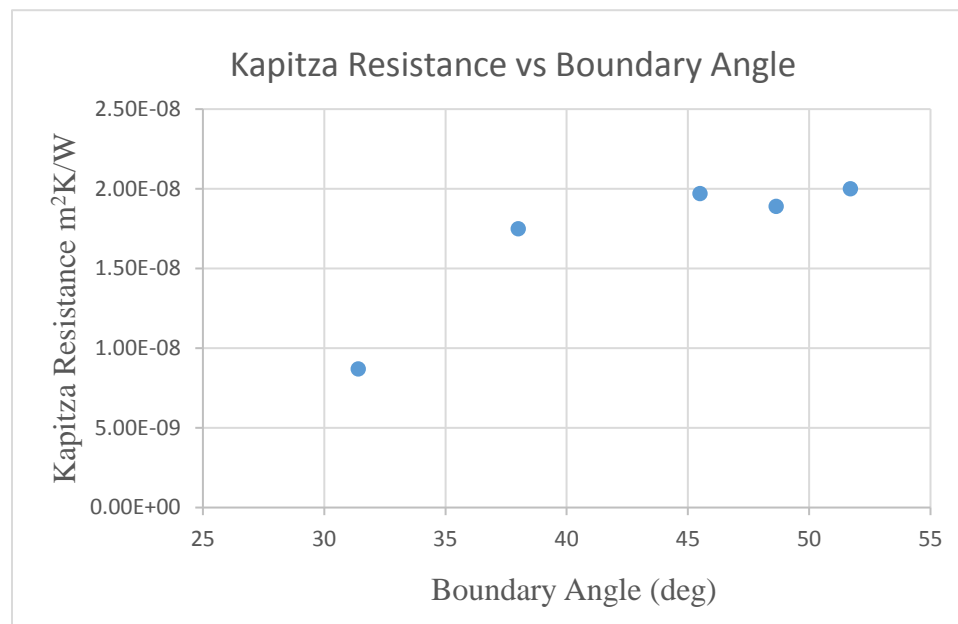nd can be used to measure more boundary angles. Finding the correlation between the boundary angles and the measured Kapitza resistances using the SSPRT is the next logical step for this type of study.

Other potential work would be to further validate the experimental measurements of this study using other methods, such as the effective medium technique. This process would involve inserting the overall thermal conductivity of the sample pellet and the intrinsic thermal conductivity of a single grain into Equation 2.1 to calculate the average Kapitza resistance. The SSPRT can still be used to measure the phase profile and thermal diffusivity, but it would be used at the center of a grain and would not come into contact with a grain boundary. This would possibly help with reducing experimental error by reducing the sensitivity that comes into play when subtracting the background from a phase profile and determining the phase drop. Because the phase drop had a larger impact on the Kapitza resistance, especially at higher phase drops, it would be interesting to see what kind of results would be measured by using alternate methods. However, this process would only be able to determine the average Kapitza resistance and not the

thermal resistance across individual interfaces. If individual Kapitza resistances are desired in order to compare them to their respective grain boundary angles, then a different process other than the effective medium method would be necessary.

Further work could be done to explore the Kapitza resistance as a function of temperature or porosity. All measurements in this thesis study were performed at room temperature and at a single porosity. It would be interesting to see the relationship between the thermal boundary resistance and higher temperatures, especially since much of the motivation for this experiment is to improve nuclear applications, which typically involve extreme temperatures.

An additional potential work would be to perfect the current system and limit sensitivity error and experimental error as much as possible. This could be done by using different equipment such as better lasers or different settings. Also, a sample that hasn't been subjected to Kr implantation and thus has significantly fewer voids could help reduce experimental error.

REFERENCES

[1]   Bergman, T., Incropera, F., Lavine, A., and DeWitt, D., 2011, *Fundamentals of Heat and Mass Transfer*.

[2]   III, W. A. G., Brenner, D. W., Lyshevsk, S. E., and Iafrate, G. J., 2003, *Handbook of Nanoscience, Engineering, and Technology*.

[3]   Berman, R., 1976, *Thermal Conductivity in Solids*, Clarendon Press, Oxford.

[4]   Swartz, E. T., and Pohl, R. O., 1989, "Thermal Boundary Resistance," Rev. Mod. Phys., **61**(3), pp. 605–668.

[5]   Carslaw, H., and Jaerger, J., *Thermal Conductivity in Solids*, Clarendon, Oxford.

[6]   Ferguson, C. D., 2011, *Nuclear Energy: What Everyone Needs to Know*, Oxford University Press, Cary.

[7]   Callister, Jr., W. D., and Rethwisch, D. G., 2010, *Materials Science and Engineering an Introduction*, Jon Wiley & Sons.

[8]   "No Title" [Online]. Available: https://en.wikipedia.org/wiki/Grain_boundary.

[9]   "No Title" [Online]. Available: http://snf.esc.cam.ac.uk/. [Accessed: 05-Dec-2017].

[10]   Kapitza, P. L., 1941, "No Title," J. Phys.-Moscow.

[11]   Smith, D., and Fayette, S., 2003, "Thermal Resistance of Grain Boundaries in Alumina Ceramics and Refractories," Am. Ceram. Soc., **11**(187409), pp. 105–111.

[12]   Klemens, P. G., 1994, "Phonon Scattering and Thermal Resistance due to Grain Boundaries," Int. J. Thermophys., **15**(6), pp. 1345–1351.

[13]   Pickett, W. E., Feldman, J. L., and Deppe, K., 1996, "Thermal Transport across Diamond Structure Materials," Model. Simul. Mater. Sci. Eng., **4**.

[14]   Schelling, P. K., Phillpot, S. R., and Keblinski, P., 2002, "Comparison of Atomic-Level Simulation Methods for Computing Thermal Conductivity," Phys. Rev. B, **65**(14), p. 144306.

[15]   Nan, C.-W., and Birringer, R., 1998, "Determining the Kapitza Resistance and the Thermal Conductivity of Polycrystals: A Simple Model," Phys. Rev. B, **57**(14), pp. 8264–8268.

[16]   Limarga, A. M., and Clarke, D. R., 2011, "The Grain Size and Temperature Dependence of the Thermal Conductivity of Polycrystalline, Tetragonal Yttria-Stabilized Zirconia," Appl. Phys. Lett.

[17]   Mogensen, M., Sammes, N. M., and Tompsett, G. A., 2000, "Physical, Chemical

and Electrochemical Properties of Pure and Doped Ceria," Solid State, **129**(1–4), pp. 63–94.

[18] Yashima, M., Kobayashi, S., and Yasui, T., 2006, "Crystal Structure and the Structural Disorder of Ceria from 40 to 1497 Degrees C," Solid State Ionics, **177**(3–4), pp. 211–215.

[19] Branda, M. M., Loschen, C., Neyman, K. M., and Illas, F., 2008, "Atomic and Electronic Structure of Cerium Oxide Stepped Model Surfaces," J. Phys. Chem. C, **112**(45), pp. 17643–17651.

[20] Nelson, A. T., Rittman, D. R., White, J. T., Dunwoody, J. T., Kato, M., and McClellan, K. J., 2014, "An Evaluation of the Thermophysical Properties of Stoichiometric CeO2 in Comparison to UO2 and PuO2," Am. Ceram. Soc.

[21] Khafizov, M., Park, I. W., Chernatynskiy, A., He, L., Lin, J., Moore, J. J., Swank, D., Lillo, T., Phillpot, S. R., El-Azab, A., and Hurley, D. H., 2014, "Thermal Conductivity in Nanocrystalline Ceria Thin Films," J. Am. Ceram. Soc., **97**(2), pp. 562–569.

[22] "No Title" [Online]. Available: http://www.reade.com/products/cerium-oxide-powder-ceo2. [Accessed: 05-Dec-2017].

[23] Yang, H. S., Bai, G. R., Thompson, L. J., and Eastman, J. A., 2002, "Interfacial Thermal Resistance in Nanocrystalline Yttria-Stabilized Zirconia," *Acta Materialia*, pp. 2309–2317.

[24] Hurley, D. H., Khafizov, M., and Shinde, S. L., 2011, "Measurement of the Kapitza Resistance across a Bicrystal Interface," J. Appl. Phys., **109**(8).

[25] Hu, C., Kiene, M., and Ho, P. S., 2001, "Thermal Conductivity and Interfacial Thermal Resistance of Polymeric Low K Films," Appl. Phys. Lett., **79**(25), pp. 4121–4123.

[26] Watanabe, T., Sinnott, S. B., Tulenko, J. S., Grimes, R. W., Schelling, P. K., and Phillpot, S. R., 2008, "Thermal Transport Properties of Uranium Dioxide by Molecular Dynamics Simulations," J. Nucl. Mater., **375**(3), pp. 388–396.

[27] Khafizov, M., and Hurley, D. H., 2011, "Measurement of Thermal Transport Using Time-Resolved Thermal Wave Microscopy," J. Appl. Phys., **110**(8).

[28] Rosencwaig, A., 1975, "Theory of the Photoacoustic Effect with Solids," J. Acoust. Soc. Am., **58**(S1), p. S52.

[29] Parker, W. J., Jenkins, R. J., Butler, C. P., and Abbott, G. L., 1961, "Flash Method of Determining Thermal Diffusivity, Heat Capacity, and Thermal Conductivity," J. Appl. Phys., **32**(9), pp. 1679–1684.

[30] Olmstead, M. A., Amer, N. M., Kohn, S., Fournier, D., and Boccara, A. C., 1983, "Photothermal Displacement Spectroscopy: An Optical Probe for Solids and

Surfaces," Appl. Phys. A Solids Surfaces, **32**(3), pp. 141–154.

[31] Lepoutre, F., Balageas, D., Forge, P., Hirschi, S., Joulaud, J. L., Rochais, D., and Chen, F. C., 1995, "Micron-Scale Thermal Characterizations of Interfaces Parallel or Perpendicular to the Surface," J. Appl. Phys., **78**(4), pp. 2208–2223.

[32] Boccara, A. C., Fournier, D., and Badoz, J., 1980, "Thermo-Optical Spectroscopy: Detection by The 'mirage Effect,'" Appl. Phys. Lett., **36**(2), pp. 130–132.

[33] Koh, Y. K., Singer, S. L., Kim, W., Zide, J. M. O., Lu, H., Cahill, D. G., Majumdar, A., and Gossard, A. C., 2009, "Comparison of the 3ω Method and Time-Domain Thermoreflectance for Measurements of the Cross-Plane Thermal Conductivity of Epitaxial Semiconductors," J. Appl. Phys., **105**(5).

[34] Paddock, C. A., and Eesley, G. L., 1986, "Transient Thermoreflectance from Thin Metal Films," J. Appl. Phys., **60**(1), pp. 285–290.

[35] Hua, Z., Ban, H., and Hurley, D. H., 2015, "The Study of Frequency-Scan Photothermal Reflectance Technique for Thermal Diffusivity Measurement," Rev. Sci. Instrum.

[36] Hartmann, J., Voigt, P., and Reichling, M., 1997, "Measuring Local Thermal Conductivity in Polycrystalline Diamond with a High Resolution Photothermal Microscope," J. Appl. Phys., **81**(7), p. 2966.

[37] Li, B., Roger, J. P., and Fournier, D., 1999, "Complete Thermal Characterization of Film-on-Substrate System by Modulated Thermoreflectance Microscopy and Multiparameter Fitting," J. Appl. Phys., **86**(9).

[38] Hua, Z., Ban, H., Khafizov, M., Schley, R., Kennedy, R., and Hurley, D. H., 2012, "Spatially Localized Measurement of Thermal Conductivity Using a Hybrid Photothermal Technique," J. Appl. Phys., **111**(10).

[39] Maznev, A. A., Hartmann, J., and Reichling, M., 1995, "Thermal-Wave Propagation in Thin-Films on Substrates," J. Appl. Phys., **78**(9), pp. 5266–5269.

[40] Khafizov, M., Chauham, V., Wang, Y., Riyad, F., Hang, N., and Hurley, D. H., 2017, "Investigation of Thermal Transport in Composites and Ion Beam Irradiated Materials for Nuclear Energy Applications," J. Mater. Res., **32**(1), pp. 204–216.

[41] Hua, Z., and Ban, H., 2017, "A New Measurement Approach for Interface Thermal Resistance Using Frequency-Scan Photothermal Reflectance Technique," Int. J. Therm. Sci., **117**, pp. 59–67.

[42] Almond, D. P., and Patel, P. M., 1996, *Photothermal Science and Techniques*, Chapman & Hall, London.

[43] SanchezLavega, A., Forge, P., Salazar, A., and Ocariz, A., 1996, "Photothermal Mirage Characterization of Vertical Interfaces Separating Two Different Media," J. Appl. Phys., **79**(2), pp. 599–608.

[44]   Mansanares, A. M., Velinov, T., Bozoki, Z., Fournier, D., and Boccara, A. C., 1994, "Photothermal Microscopy: Thermal Contrast at Grain Interface in Sintered Metallic Materials," J. Appl. Phys., **75**(7).

[45]   "No Title" [Online]. Available: https://dir.indiamart.com/impcat/cerium-oxide-powder.html.

[46]   Cao, A., and Qu, J., 2012, "Kapitza Conductance of Symmetric Tilt Grain Boundaries in Graphene," J. Appl. Phys., **111**(5).

[47]   Tai, K., Lawrence, A., Harmer, M. P., and Dillon, S. J., 2013, "Misorientation Dependence of Al2O3 Grain Boundary Thermal Resistance," Appl. Phys. Lett.